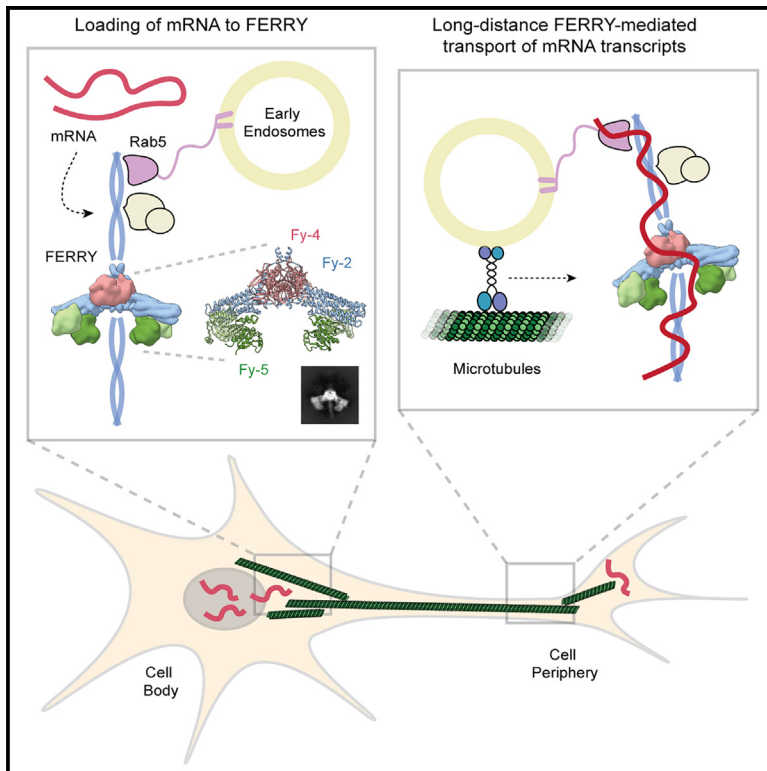


Structural basis of mRNA binding by the human FERRY Rab5 effector complex

Graphical abstract



Authors

Dennis Quentin, Jan S. Schuhmacher, Björn U. Klink, ..., Henning Urlaub, Marino Zerial, Stefan Raunser

Correspondence

zerial@mpi-cbg.de (M.Z.), stefan.raunser@mpi-dortmund.mpg.de (S.R.)

In brief

The cryo-EM structure of the pentameric FERRY Rab5 effector complex in Quentin, Schuhmacher et al. sheds light on the elusive link between mRNA and early endosomes in long-range transport of transcripts. Its unique clamp-like architecture is closely linked to a novel mode of RNA binding, involving its terminal coiled-coil domains.

Highlights

- FERRY links mRNA to early endosomes in long-range transport of transcripts
- Unique clamp-like architecture of the pentameric FERRY Rab5 effector complex
- Complex RNA binding interface mainly involves flexible coiled-coil domains of Fy-2
- Neurological disorder-related mutations impair Rab5 binding and FERRY assembly



Article

Structural basis of mRNA binding by the human FERRY Rab5 effector complex

Dennis Quentin,^{1,8} Jan S. Schuhmacher,^{2,8} Björn U. Klink,^{1,3} Jeni Lauer,² Tanvir R. Shaikh,^{1,7} Pim J. Huis in 't Veld,⁴ Luisa M. Welp,⁵ Henning Urlaub,^{5,6} Marino Zerial,^{2,*} and Stefan Raunser^{1,9,*}

¹Department of Structural Biochemistry, Max Planck Institute of Molecular Physiology, 44227 Dortmund, Germany

²Max Planck Institute of Molecular Cell Biology and Genetics, 01307 Dresden, Germany

³Center for Soft Nanoscience and Institute of Molecular Physics and Biophysics, 48149 Münster, Germany

⁴Department of Mechanistic Cell Biology, Max Planck Institute of Molecular Physiology, 44227 Dortmund, Germany

⁵Max Planck Institute for Multidisciplinary Sciences, 37077 Göttingen, Germany

⁶Institute of Clinical Chemistry, University Medical Center Göttingen, 37075 Göttingen, Germany

⁷Present address: Institute of Neuropathology, University of Göttingen Medical Center, 37077 Göttingen, Germany

⁸These authors contributed equally

⁹Lead contact

*Correspondence: zerial@mpi-cbg.de (M.Z.), stefan.raunser@mpi-dortmund.mpg.de (S.R.)

<https://doi.org/10.1016/j.molcel.2023.05.009>

SUMMARY

The pentameric FERRY Rab5 effector complex is a molecular link between mRNA and early endosomes in mRNA intracellular distribution. Here, we determine the cryo-EM structure of human FERRY. It reveals a unique clamp-like architecture that bears no resemblance to any known structure of Rab effectors. A combination of functional and mutational studies reveals that while the Fy-2 C-terminal coiled-coil acts as binding region for Fy-1/3 and Rab5, both coiled-coils and Fy-5 concur to bind mRNA. Mutations causing truncations of Fy-2 in patients with neurological disorders impair Rab5 binding or FERRY complex assembly. Thus, Fy-2 serves as a binding hub connecting all five complex subunits and mediating the binding to mRNA and early endosomes via Rab5. Our study provides mechanistic insights into long-distance mRNA transport and demonstrates that the particular architecture of FERRY is closely linked to a previously undescribed mode of RNA binding, involving coiled-coil domains.

INTRODUCTION

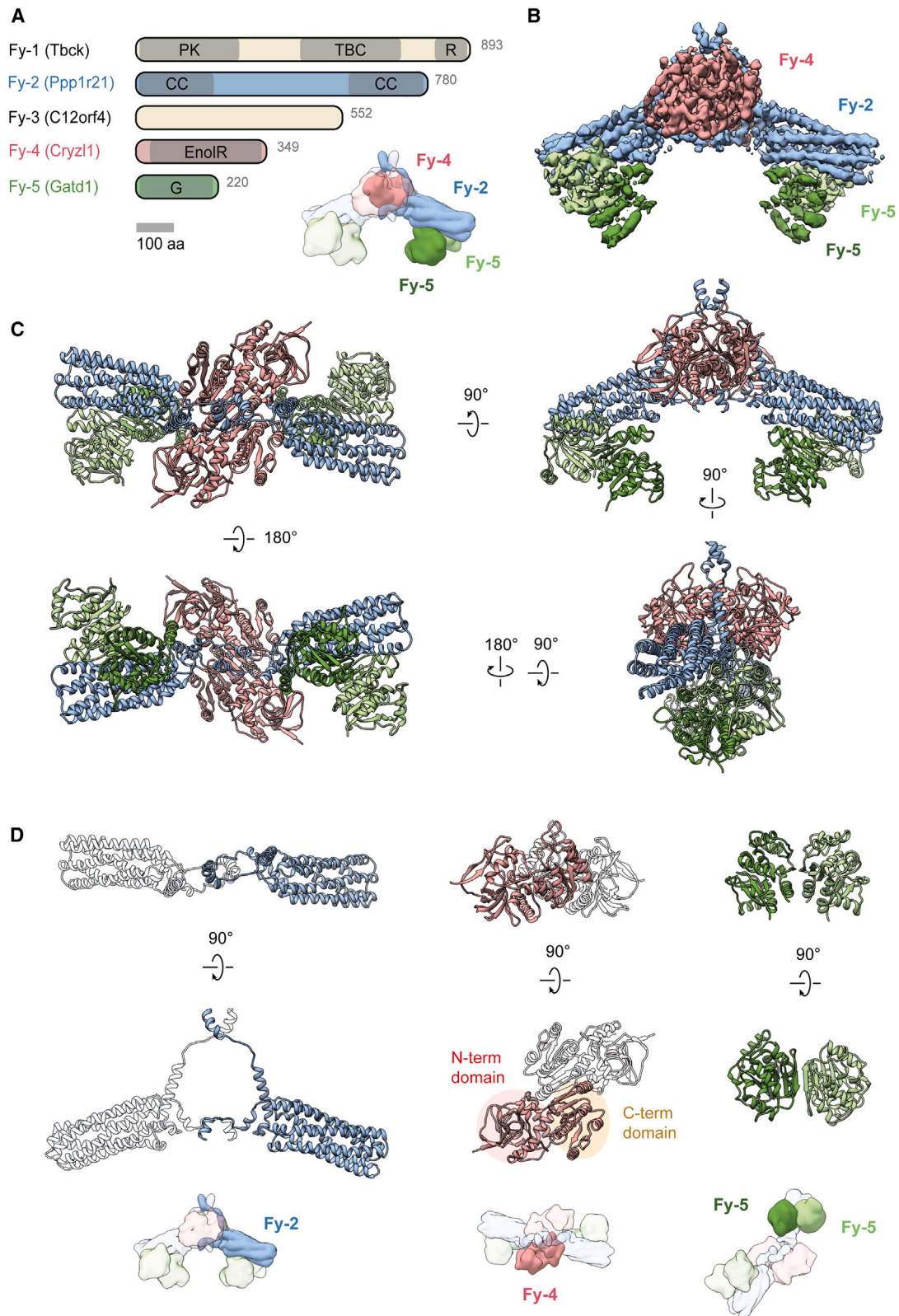
Rab small GTPases are master regulators of intracellular transport^{1–3} that contribute to the structural and functional integrity of organelles. In the GTP-bound conformation, membrane-associated Rab proteins can recruit a plethora of diverse downstream effector proteins to accomplish membrane remodeling activities.^{1–4}

Rab5, one of the most extensively studied small GTPases, is mainly localized at the early endosome (EE) and regulates endocytosis and EE dynamics.⁵ The vast network of interaction partners of Rab5⁶ includes GEFs, like Rabex-5 and RIN1,^{6,7} but also Rab5-specific GAPs such as RN-Tre⁸ and Rab-GAP5.⁹ Prominent effectors like Rabaptin-5, Rabankyrin-5, Rabenosyn-5, EEA1, and APPL1/2 act downstream and can bind Rab5 via distinct domains such as zinc fingers.^{10–14} Co-structures of Rab effectors bound to their cognate GTPase, including Rab5-Rabaptin-5, and Rab4-Rabenosyn-5, have provided important insights in the functional interactions between Rab proteins and their effectors and regulators,^{15–17} demonstrating that binding is typically mediated by the switch and inter-switch regions of Rab proteins and either symmetric coiled-coils or α -helical bun-

dles of effectors. In addition to individual proteins, Rab effectors comprise large multiprotein complexes, such as Exocyst and HOPS, that mediate crucial functions in the exocytic and endocytic pathways.^{18–21} These multiprotein complexes are non-symmetric, highly flexible and dynamic, and therefore challenging to analyze structurally. Hence, known structures are often limited to the core of the complexes, and it is difficult to reach high resolution.^{18,19,22}

Rab5 is also implicated in long-range endosomal motility.²⁰ By harnessing the intracellular microtubule (MT) network, EEs can be actively transported via MT motor complexes to distal locations within the cell.²³ Recent evidence suggests a role of endosomal motility also in RNA localization and expression. RNA transport and local translation serves as a prime example of how spatiotemporal control can influence the expression of genes underlying essential biological processes, such as embryonic development or neuronal plasticity.^{21,24} Local sites individually regulate gene expression, which is thus not limited to transcriptional control in the nucleus. The sophisticated mRNA localization pattern observed in polarized cells like neurons requires active transport of transcripts. Studies in a number of model systems, including yeast and *Drosophila melanogaster*,





(legend on next page)

have identified components of the RNA transport machinery, both at the level of the mRNA and localization machinery.²⁵ First, the pattern of localization depends on specific RNA elements, often positioned in the 3'UTR of the mRNA.^{23,26,27} Second, two distinct active transport pathways, both exploiting the cytoskeletal network in combination with motor proteins, have emerged: RNA is transported with the help of accessory proteins, termed *trans*-acting proteins, that bind RNA to form ribonucleoprotein particles (RNPs).²⁶ These proteins can contain specific RNA binding domains. Alternatively, mRNA can be associated with endosomal compartments, both actively transported by co-opting cytoskeletal components.^{28–30} In this case, the molecular interactions mediating mRNA binding to organelles are unknown. The role of late endosomes and lysosomes in mRNA localization has been subject of recent research, where Annexin 11A has been proposed to mediate the association between RNA and lysosomes.³⁰ While these initial insights are valuable, they are limited to a subclass of the endocytic system. In filamentous fungi, mRNA localization is mediated by the microtubule-based transport of vesicles, including EEs.³¹ In neurons, long range transport of various types of cargo, including mRNA, requires active transport, which is mediated by endocytic organelles, particularly late endosomes.^{28,32} However, mechanisms must ensure the localization of mRNA distant from the cell body, such as in dendrites and axons in neurons, as late endocytic organelles undergo bidirectional but primarily minus-end microtubule-directed motility.³³ Candidate organelles for localizing mRNAs to the periphery of processes in neurons are also early endosomes.³⁴ However, little is known whether and how mRNAs are transported via early endosomes to their target destination.

We have identified a human 5-subunit Rab5 effector complex termed five-subunit early endosomal Rab5 and RNA/ribosome intermediary (FERRY) complex,³⁵ which interacts with mRNA and thus represents a prime candidate for early endosome-mediated mRNA transport. The FERRY complex is composed of Tbc (Fy-1), Ppp1r21 (Fy-2), C12orf4 (Fy-3), Cryz11 (Fy-4), and Gatd1 (Fy-5), which have a molecular weight of 101, 88, 64, 39, and 23 kDa, respectively (Figure 1A). Here, we determined the cryoelectron microscopy (cryo-EM) structure of the FERRY complex at a resolution of 4 Å. Together with rotary-shadowing EM, hydrogen-deuterium exchange mass spectrometry (HDX-MS), crosslinking mass spectrometry (MS), electrophoretic mobility shift assay (EMSA) and mutational studies, the structure demonstrates that FERRY is an elongated complex with a clamp-like architecture at its center and protruding flexible coiled-coil structures at its periphery that mediate the interaction with the EE via Rab5 and mRNA. Moreover, the combination of biochemical and structural studies allowed us to delineate the complex RNA binding interface of FERRY, which is composed

of the two-opposing coiled-coils of the central hub protein Fy-2 as well as Fy-5, shedding light on how FERRY links mRNA to early endosomes in long-range transport of transcripts.

RESULTS

Architecture of the FERRY Rab5 effector complex

To understand the interaction of the five subunits of FERRY in molecular detail, we expressed and purified the subunits as described in Schuhmacher et al.³⁵ (see STAR Methods) and reconstituted the complex *in vitro* (Figure S1). We then determined the cryo-EM structure of FERRY to an overall resolution of 4.0 Å, applying C2 symmetry (Figures 1B, S2, and S3; Table 1). The structure reveals that the core of FERRY is composed of a dimer of Fy-4, two molecules of Fy-2 and four copies of Fy-5, resulting in a 2:2:4 stoichiometry (Figures 1B and S2). The other two subunits, namely Fy-1 and Fy-3, were not resolved in the structure, although SDS-PAGE analysis clearly confirmed their presence in the complex (Figure S1). The mass of the FERRY complex determined by mass photometry (Schuhmacher et al.³⁵ and Figure S5) together with the intensities of the corresponding signals of a Coomassie stained SDS-PAGE gel³⁵ suggests that only a single Fy-1 and Fy-3 bind to the dimeric arrangement of the FERRY core, resulting in a ratio of 1:2:1:2:4 (Fy-1:Fy-2:Fy-3:Fy-4:Fy-5) for the whole complex.

The high quality of the cryo-EM map allowed us to build atomic models for Fy-2 and Fy-4 into the corresponding densities (Figures 1B–1D; Table 1). Densities corresponding to the four Fy-5 molecules, located at the periphery of the reconstruction, exhibited lower local resolution. To obtain an atomic model for these regions, we initially solved the X-ray structure of Fy-5 at 2.7 Å resolution (Table 2) and subsequently relaxed it into the density (Figures 1C, 1D, and S3; Tables 1 and 2).

The structure of the FERRY core reveals an overall clamp-like architecture with two arm-like appendages emanating in opposite directions from a central bulky body (Figures 1B, 1C, S2, and S3). Two Fy-4 molecules assemble as a symmetrical dimer, forming the central body of FERRY (Figure 1D). Each monomer adopts a Rossmann-like fold, where 6 β-strands and 6 α-helices alternate. Through dimerization, a continuous 12-stranded twisted β-sheet encased by two layers of α-helices is formed, which is a typical feature of dimeric enoyl reductases. The N-terminal part of Fy-4 is homologous to the catalytic domain of enoyl reductases. Although Fy-4 is equipped with the full set of catalytic residues for enzymatic activity, the location in the center of the complex embraced by helices of Fy-2 blocks the substrate binding site. Thus, a potential catalytic activity of Fy-4 is inhibited in this conformation. However, since human enoyl reductases are normally found as part of the fatty acid synthase complex,³⁶

Figure 1. Architecture of the FERRY complex

(A) Domain architecture of the FERRY complex. Schematic representation of the FERRY core (bottom right) with only one-half of the symmetric complex highlighted. PK, pseudokinase; TBC, Tre-2/Bub2/Cdc16; R, rhodanese; CC, coiled-coil; EnolR, enoyl reductase; G, GATase1-like domain. (B) Segmented cryo-EM density map of the FERRY core. Fy-2 (blue), Fy-4 (red), and Fy-5 (green). Proximal and distal Fy-5 are colored in dark and light green. (C) Rotated views of the atomic model of FERRY with subunits colored according to (B). (D) Rotated views of individual subunits of the FERRY core with Fy-2, Fy-4, and Fy-5 shown on the left, middle, and right, respectively. In case of Fy-2 and Fy-4, dimeric partner is indicated as transparent ribbon representation. The relative location within the complex is highlighted in the cartoon representation below. See Figures S1–S3 and Tables 1 and 2.

Table 1. Data collection, refinement and model building statistics of FERRY cryo-EM structures, related to Figure 1

Microscopy and cryo-EM	C2	C1
Microscope	Titan Krios	Titan Krios
Voltage [kV]	300	300
Camera	K2 Summit	K2 Summit
Defocus range [μm]	−1.6 to −2.8	−1.6 to −2.8
Pixel size [\AA]	1.08	1.08
Total electron dose [$\text{e}^-/\text{\AA}^2$]	75.8	75.8
Exposure time [s]	15	15
Frames per Movie	40	40
Number of micrographs	1,879	1,879
Number of particles in final reconstruction	18,300	18,300
Map resolution [\AA]	4.0	6.2
Model statistics		
Bond RMSD [\AA]	0.011	
Angle RMSD [$^\circ$]	1.66	
Rotamer outliers [%]	0.21	
Ramachandran—favored [%]	94.63	
Ramachandran—allowed [%]	5.05	
Ramachandran—outliers [%]	0.32	
Molprobrity score	1.96	
EMRinger score	1.24	

which catalyzes the last step of fatty acid synthesis, a similar enzymatic function of Fy-4 in the context of the FERRY complex seems rather unlikely.

The arm-like appendages of FERRY are formed by a 6-helix bundle of Fy-2 and a Fy-5 dimer each (Figures 1B–1D). The Fy-2 molecules embrace the central Fy-4 dimer and dimerize at their N- and C-terminal ends as coiled-coils, of which only the stem is resolved to high resolution (Figures 1B–1D). The unique architecture of FERRY, which is likely intimately linked to its function as mRNA transport vehicle, does not resemble any of the described large Rab effector complexes, suggesting that FERRY represents a new class of multiprotein Rab effector complex.

Fy-2 serves as central scaffolding protein

Fy-2 adopts an integral position within the FERRY complex, as it directly interacts with all other subunits. In the FERRY core, Fy-2 connects Fy-4 and Fy-5 and thereby acts as a scaffold for assembly of the whole protein complex (Figures 2A and 2B). The 6-helix bundle of Fy-2 (aa 246–498) is folded in such a way that its antiparallel α -helices form a 5 nm-long hollow tube (Figure 2A).

The interaction of Fy-2 with Fy-5 is mediated by the 6-helix bundle (Figures 2B and 2C). Similar to Fy-4, Fy-5 contains a Rossmann-like fold, composed of a central 6-stranded β -sheet surrounded by six α -helices, and dimerization of Fy-5 results in a continuous 12-stranded twisted β -sheet (Figure 1D). The proximal and distal Fy-5 subunits bind to helices 4–5 and 2–3 of the 6-helix bundle, respectively, and form a relatively planar inter-

face (Figures 2B and 2C). Interestingly, although the 6-helix bundle is non-symmetrical, the interface between the Fy-5 dimer and the 6-helix bundle has a pseudo-two-fold symmetry (Figures 2C and S3). The interaction between Fy-5 and the 6-helix bundle of Fy-2 is dominated by charge complementarity (Figure 2D). While Fy-2 is enriched in positively charged residues at the interface, Fy-5 features a negatively charged patch. These findings are further corroborated by HDX-MS studies showing reduced deuterium exchange in the Fy-2 binding region of Fy-5 as well as in most of the corresponding binding regions of Fy-2 (Figures 2E and S4).

To find out whether the interaction of Fy-5 with Fy-2 alters its conformation, we compared our 2.7 \AA crystal structure of Fy-5 with Fy-5 in the cryo-EM structure (Figure 2F; Table 2). Similar to the cryo-EM structure of the complex, Fy-5 formed symmetric dimers and the structure of the major part of the protein was identical (RMSD: 0.812 \AA , Figure 2F). However, the Fy-2 binding region of Fy-5 (aa 152–184) was rotated in-plane by $\sim 40^\circ$. Interestingly, this rotation happens in both subunits, so that the dimer stays symmetric and increases the binding interface between the two proteins.

The regions flanking the 6-helix bundle (aa 226–245 and aa 512–540) closely interact with the Fy-4 dimer by wrapping it with extended linkers, including a prominent vertical helix (Figures 2A and 2B). Both linkers localize either to clefts or grooves at the protomer-protomer interface of the Fy-4 dimer forming tight interactions based on charge as well as shape complementarity (Figures 3A and 3B). This complementarity is particularly prominent in the C-terminal linker where it even extends all the way to the start of the C-terminal coiled-coil domain. A striking feature of the interface between the N-terminal linker and Fy-4 are two electrostatic clusters with up to three different subunits participating. The first cluster comprises Lys-225 and Glu-224 from one Fy-2 molecule, Asp-230 from the second Fy-2, and Lys-299 from Fy-4 (Figure 3B). The second cluster is formed by Lys-232 of Fy-2 and Asp-306 and Glu-309 and Lys-310 of Fy-4.

The tight interaction between Fy-2 and Fy-4 becomes also evident from HDX-MS measurements (Figures 3C and S4). Except for residues 237 to 250, for which no peptides were detected, all parts of Fy-2 that are in close contact with Fy-4 showed a decrease in deuterium uptake in the presence of Fy-4, indicating lower accessibility upon complex formation. The same is true for regions forming the binding clefts of Fy-4.

To investigate the effect of Fy-2 binding to Fy-4, we crystallized the Fy-4 dimer in the absence of Fy-2, solved its structure at 2.9 \AA resolution, and compared it with our cryo-EM structure of the complex (Figures 3D and 3E; Table 2). While the overall structural similarity is high (RMSD: 0.766 \AA), we observed two major differences between the two structures. First, the loop of Fy-4 (aa 293–297) moves slightly sideways to accommodate the vertical helix of Fy-2 upon complex formation (Figure 3D). The second and more striking difference occurs in the region 225–239 of Fy-4, located close to the C-terminal coiled-coil of Fy-2. Here, a previously flexible loop of Fy-4 moves toward Fy-2 to form an additional interface, thereby strengthening the interaction between the two molecules (Figure 3E).

Table 2. Data collection, refinement, and model building statistics of X-ray structures, related to Figure 1

Data collection	Fy-5	Fy-4
Space group	C222(1)	P2
a, b, c, [Å]	94.62 99.57 62.12	86.42 45.27 93.96
α, β, γ [Å]	90 90 90	90 109.93 90
Energy [keV]	12.81	12.81
Resolution [Å]	47.31–2.7	45.92–2.9
Inner shell	2.85–2.6	3.06–2.9
R_{merge}	0.088 (0.603)	0.056 (0.209)
$I/\sigma(I)$	13.4 (3.2)	17.9 (6.2)
Completeness [%]	99.6 (99.9)	99.1 (99.7)
Redundancy	9.6 (10.1)	4.9 (5.0)
$CC_{1/2}$	0.997 (0.970)	0.996 (0.974)
Refinement	Fy-5	Fy-4
Resolution [Å]	2.7	2.9
No. reflections	8324	15371
$R_{\text{work}}/R_{\text{free}}$	22.0/26.7	23.7/28.5
No. Atoms	Fy-5	Fy-4
Protein	1,426	4,954
Ligand	0	0
Water	0	21
R.m.s deviations	Fy-5	Fy-4
Bond lengths [Å]	0.006	0.004
Bond angles [°]	0.894	0.709
Ramachandran	Fy-5	Fy-4
Ramachandran—favored [%]	95.8	95.0
Ramachandran—allowed [%]	4.2	4.7
Ramachandran—outliers [%]	0	0.3

The N- and C-terminal regions of the two Fy-2 subunits, namely upstream of aa 226 and downstream of aa 540, engage with their respective counterparts to form elongated coiled-coil structures that extend from the complex in diametrically opposite directions. However, the absence of a clear density for the majority of the coiled-coils in our structure indicates flexibility of these domains.

Role of the two terminal coiled-coils of Fy-2

Our cryo-EM structure revealed the architecture of the FERRY complex core, in which Fy-2 plays a key role as central scaffolding protein. However, two complex subunits, namely Fy-1 and Fy-3, were not resolved in the cryo-EM structure. Data from integrated protein-protein interaction network tools, such as STRING, indicated a close spatial and functional connection between the two subunits.³⁷ To identify their position within the complex, we performed HDX-MS measurements in the presence and absence of various complex subunits (Figures 4A and S4). This allowed us to narrow down the binding regions of

Fy-1 and Fy-3 to residues 646–705 of Fy-2, which is located in its C-terminal coiled-coil. We further performed protein cross-linking experiments of the FERRY complex using the zero-length cross-linker 1-ethyl-3-[3-dimethylaminopropyl]carbodiimide hydrochloride (EDC) (Figures S5A–S5C; Data S2). The experiments revealed several positions on Fy-1 and Fy-3 that overlap with the ones determined by HDX-MS. In addition, we observed cross-links from both Fy-1 and Fy-3 to a region adjacent to the main binding site on Fy-2, suggesting that Fy-1 and Fy-3 likely form additional contact sites that were not detected by HDX-MS. Furthermore, differential deuterium uptake profiles in the presence and absence of the small GTPase Rab5 allowed us to delineate the Rab5 binding region on the FERRY complex. Like Fy-1/3, it is located on the C-terminal coiled-coil of Fy-2, but a bit closer to the C terminus (aa 728–752). In known structures of Rab5/Rab5-effector complexes, including those of Rabaptin-5 and EEA1, Rab5 binds via its switch and inter-switch regions either directly to coiled-coils or to regions in their proximity.^{17,38} Indeed, the Rab5 binding region in the FERRY complex is predicted to form a parallel coiled-coil, further corroborating our HDX data (Figures 4A, 4B, and S4). Due to the symmetric structure of the coiled-coil, either one or two Rab5 proteins can bind simultaneously to FERRY.

In our cryo-EM structure, we could only identify density corresponding to the first few residues of the C-terminal coiled-coil region of Fy-2 (Figures 1B, S2, and S3). This suggests a high flexibility of the rest of the coiled-coil, which is commonly observed also for other coiled-coil-containing complexes.³⁹ In general, long coiled-coils without a rigidifying interaction partner are mostly flexible and, thus, challenging to visualize in EM. To visualize the C-terminal coiled-coil region as well as the Fy-1 and Fy-3 subunits, we performed low-angle platinum shadowing experiments with the FERRY complex and extended hierarchical clustering of selected initial cryo-EM FERRY classes (Figures 4C and S6; Video S1). In the former analysis, we observed particles with two rod-like protrusions emanating from opposite sides of the FERRY core (Figures 4C and S6). These protrusions probably correspond to the two terminal coiled-coil regions of Fy-2. The extended classification of the cryo-EM data revealed a rod-like density and a globular density that can be attributed to the coiled-coil and possibly to the Fy-1/3 subunits, respectively (Figures 4C and S6; Video S1).

In the case of the N-terminal coiled-coil of Fy-2, we observed only density corresponding to the beginning of the coiled-coil at high resolution (Figures 1B, S2, and S3), similar to its C-terminal counterpart. However, at lower thresholds and, in particular, in two-dimensional (2D) class averages, we could also identify density in the space between the two arm-like appendages (Figure 4D). This density can be unambiguously identified as a coiled-coil structure, which adopts multiple orientations relative to the FERRY core (Figure 4D; Video S2). This also explains the lower resolution in this region of the complex (Figure S3). Therefore, we calculated a reconstruction of the FERRY complex without applying symmetry, yielding a 6.2 Å map (Figures 4E, S2, and S3). Although the resolution of the coiled-coil did not improve and still appeared only at a lower threshold, its rod-like appearance including a twist is reminiscent of a coiled-coil. We believe that the proximal Fy-5 molecules bound to the arm

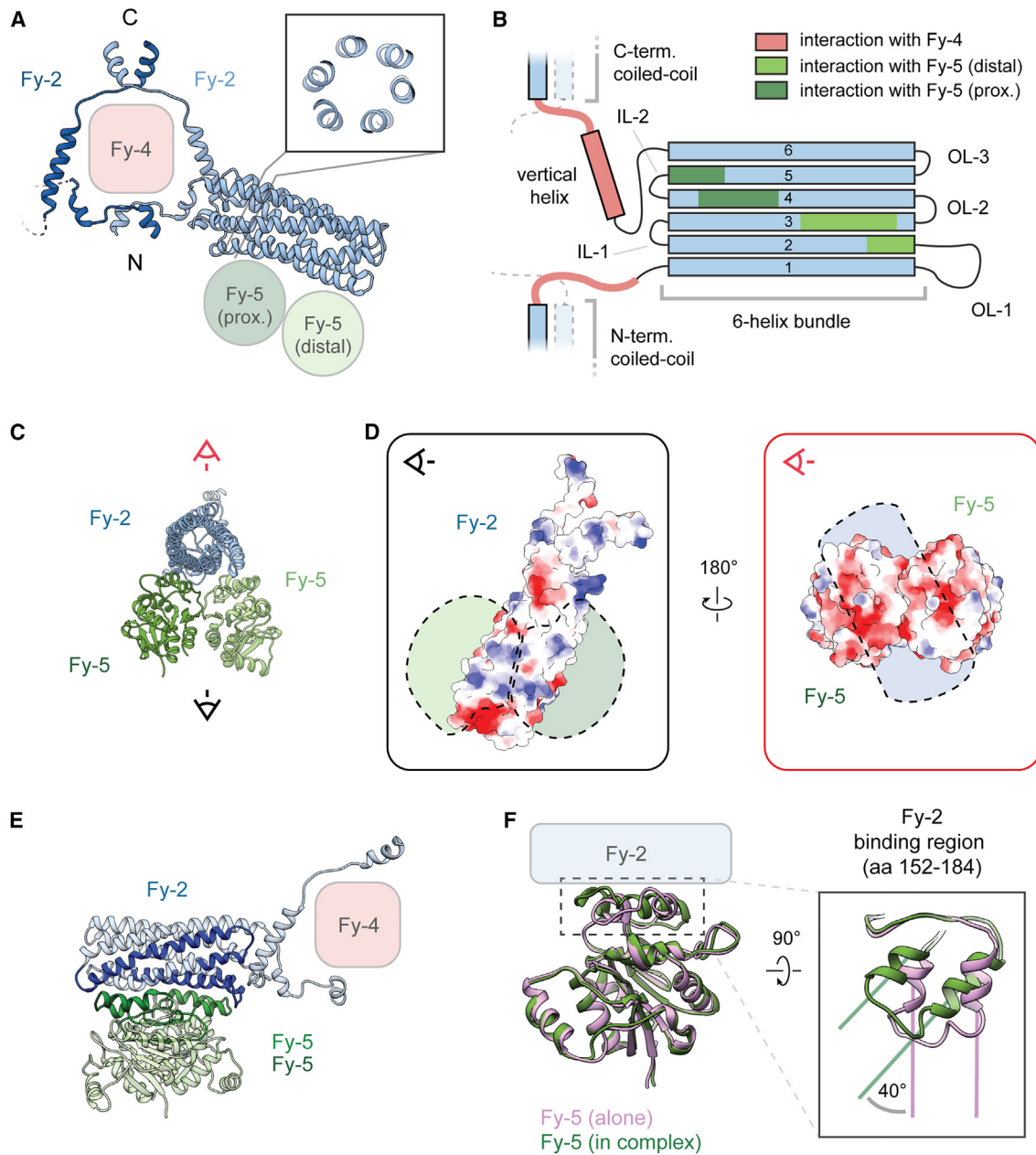


Figure 2. Interaction of Fy-2 with Fy-5

(A) Fy-2 dimerizes with the second Fy-2 subunit to form two coiled-coil regions and interacts with the Fy-5 dimer and Fy-4. A 6-helix bundle domain connects the two coiled coils. Inset shows a cross-section through the bundle.
 (B) Topology diagram depicting the domain organization of Fy-2.
 (C) Fy-5 dimer binding to the 6-helix bundle domain of Fy-2.
 (D) Bottom and top views of the interface between Fy-2 and Fy-5; surfaces are colored by electrostatic Coulomb potential from -10 kcal/mol (red) to $+10$ kcal/mol (blue).
 (E) Interacting regions of Fy-2 and Fy-5 based on HDX-MS are highlighted in dark blue and green.
 (F) Superposition of the crystal structure of Fy-5 (pink) and proximal Fy-5 bound in the FERRY complex (green). Inset shows a rotated close-up of the Fy-2-binding region of Fy-5 featuring a $\sim 40^\circ$ in-plane rotation upon Fy-2 binding. See [Figure S4](#).

restrict the overall mobility of the N-terminal coiled-coil of Fy-2 ([Figure 4F](#)). The functional implications of this restricted degree of movement, however, are not yet understood. Taken together, our results show that both terminal coiled-coil domains of Fy-2

have different degrees of flexibility and act as a binding hub for other FERRY subunits. This even further underpins the central role of Fy-2 in the FERRY complex, as it directly interacts with all other four members of the complex as well as with Rab5.

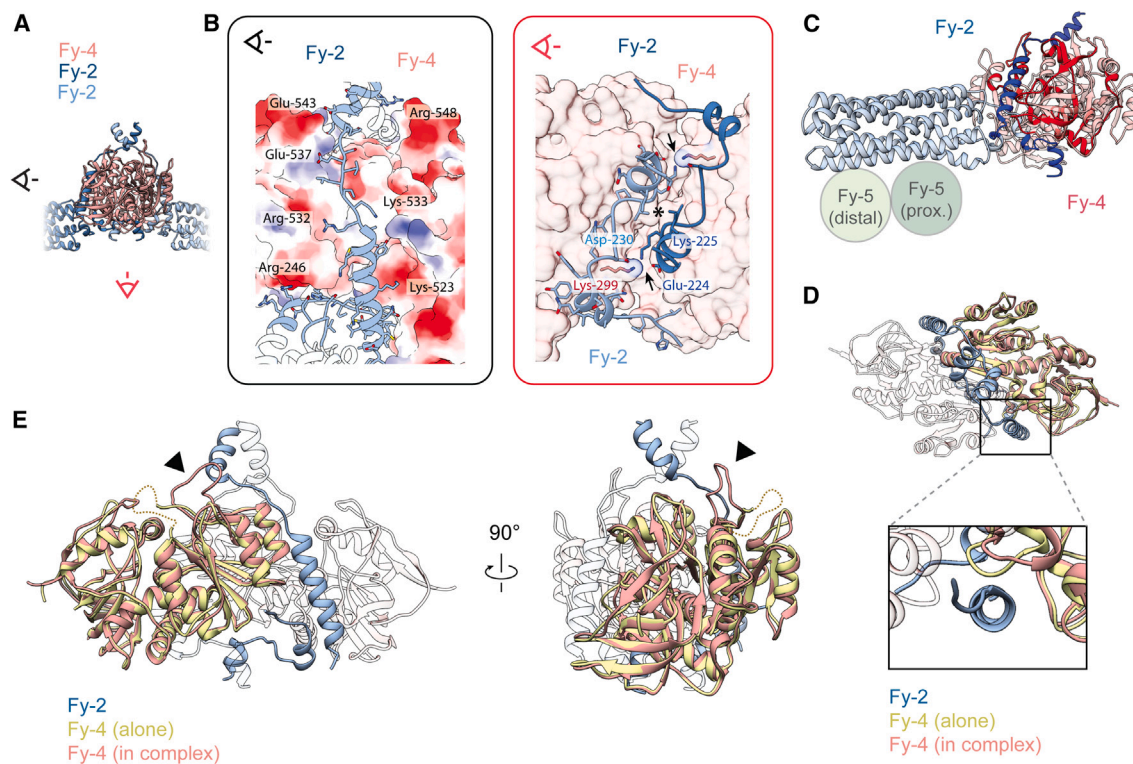


Figure 3. Interaction of Fy-2 with Fy-4

(A) Fy-2 interacts with Fy-4 by wrapping around it before dimerizing with the second Fy-2 to form coiled-coil regions. (B) Close-ups of the side view in (A). The Fy-4 dimer is presented as electrostatic surface, interacting parts of Fy-2 as blue ribbon (left). Fy-2 as ribbon in light and dark blue with important residues highlighted (right). The beginning of the N-terminal coiled-coil domain of Fy-2 is highlighted by an asterisk. The complex is stabilized by two charged clusters (black arrows), flanking the coiled-coil. (C) Interacting regions of Fy-2 and Fy-4 based on HDX-MS are highlighted in dark blue and red. (D) Top views of the superposition of the X-ray structure of Fy-4 (yellow) and Fy-4 bound in the FERRY complex (red). Inset shows a close-up of the binding cleft for the vertical helix of Fy-2 (blue), formed by the two Fy-4 protomers. Upon Fy-2 binding, a loop region of Fy-4 moves sideways to accommodate the vertical helix of Fy-2. (E) Rotated views of the superposition of the crystal structure of Fy-4 (yellow) and Fy-4 bound in the FERRY complex (red). When Fy-4 is bound in the complex, a previously disordered loop region, indicated as dotted line, becomes ordered (black arrow) and interacts with Fy-2. See [Figure S4](#).

Interaction of FERRY with mRNA

To determine whether the purified FERRY complex binds mRNA *in vitro*, we performed EMSAs with the fully reconstituted FERRY complex (Fy-1/2/3/4/5) and four different mRNAs (*mrpl41*, *mdh2*, *prdx5*, *pigl*) (Figures 5B and S7A). The results clearly show that all different mRNAs bind to FERRY. Interestingly, with increasing amounts of mRNA the signal corresponding to the FERRY-RNA complex sharpens into a band and migrates at a lower molecular weight (Figures 5B–5D and S7A–S7C). This is an indication that RNA binding decreases the structural flexibility of the complex.

A protein structure comparison using the DALI server found several members of the DJ-1/ThiJ/Pfpl superfamily to have a similar structure to Fy-5. Interestingly, DJ-1, which shares the Rossmann-like fold and overall structure with Fy-5 (RMSD: 1.012 Å; Figure S3), has been shown to bind RNA at nanomolar concentrations, and mutations in the corresponding gene have been linked to neuronal degeneration.^{40,41} The close structural similarity between both proteins suggests that Fy-5 could perform a similar function, i.e., contribute to RNA binding, in the FERRY complex. However, EMSAs showed that Fy-5 alone

does not exhibit detectable RNA binding (Figure S7D). We can envisage two possible explanations: either Fy-5 is not involved in mRNA interaction, or the interaction interface is more complex and requires different subunits of the FERRY complex simultaneously. To resolve this question, we performed UV-induced protein-RNA crosslinking-MS⁴² (Figure 5A; Data S1). The analysis revealed in total 37 lysine residues within Fy-1 to Fy-5 crosslinked to RNA (Data S1). Only two of the crosslinked lysine residues are found in one loop region of Fy-5 (Figure 5A). Unexpectedly, most crosslinks cluster along the coiled-coils of Fy-2 instead, suggesting that bound RNA stretches over the whole length of the FERRY complex or that several RNA molecules bind simultaneously to the same FERRY complex at different positions. Interestingly, several crosslink sites are located in the cavity of the clamp-like structure in the FERRY complex, suggesting that this clamp plays an important role in mRNA binding (Figure 5A). Consistent with the crosslinking data, the bottom of the cavity is lined by positively charged residues, which are known to be essential for the interaction of proteins with RNA (Figure S3).^{43,44}

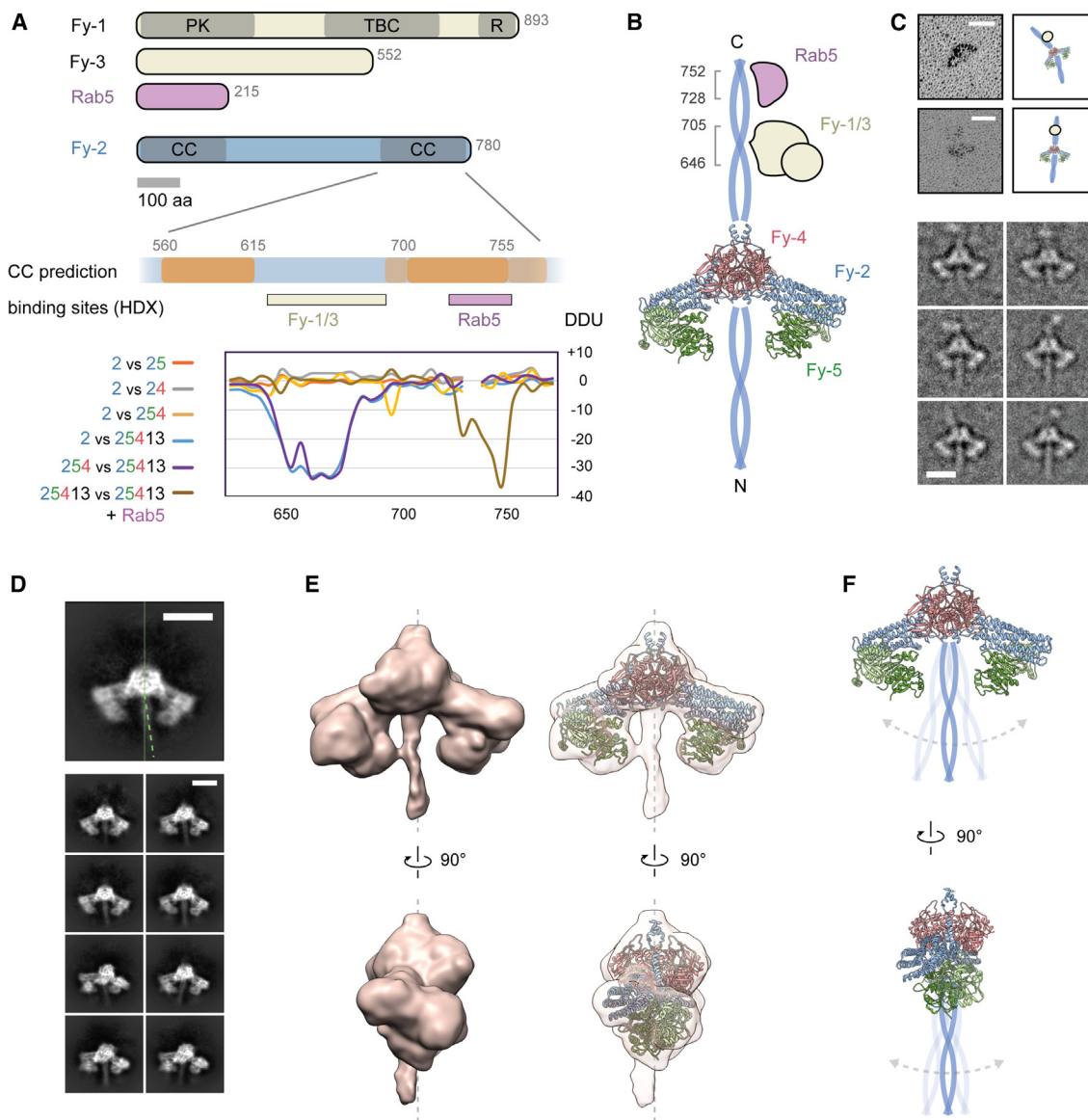


Figure 4. Terminal coiled-coil regions of Fy-2 extend in opposite directions

(A) Domain architecture of the Fy-2-interacting proteins Fy-1, Fy-3, and Rab5. Enlargement of the C-terminal domain of Fy-2 shows predicted coiled-coil regions with orange indicating high CC formation probability. HDX-MS delineates the binding regions of Fy-1/3 and Rab5 on the C-terminal coiled-coil of Fy-2. DDU, differential deuterium uptake.

(B) Schematic representation of FERRY complex. Binding sites for Fy-1/3 and Rab5 are derived from HDX-MS.

(C) FERRY visualized by EM after glycerol spraying and low-angle platinum shadowing with corresponding cartoon illustrations (upper panel). Scale bar, 20 nm. Selected 2D cryo-EM classes of FERRY show density corresponding to the C-terminal coiled-coil region of Fy-2 located at the top of the complex (bottom panel). Scale bar, 10 nm.

(D) Cryo-EM 2D class averages of FERRY illustrating that the N-terminal coiled-coil of Fy-2 adopts multiple positions relative to the FERRY core. Scale bars, 10 nm.

(E) Rotated views of 3D reconstruction of FERRY without applied symmetry, filtered to 15 Å. Right panel shows fitting of the atomic models for the FERRY core into the density for orientation. The elongated density that protrudes from the central Fy-4 dimer corresponds to the N-terminal coiled-coil of Fy-2.

(F) Schematic representation of the FERRY complex highlighting the flexible nature of the N-terminal Fy-2 coiled-coil. See [Figures S4](#) and [S6](#) and [Videos S1](#) and [S2](#).

In order to verify that Fy-2 is sufficient for RNA binding, we carried out EMSAs with the three-subunit Fy-2, Fy-4, and Fy-5 core complex. RNA bound to this complex as efficiently as to the whole FERRY complex, indicating that Fy-1 and Fy-3 are not

required for RNA binding ([Figures 5C](#) and [S7B](#)). However, when we performed the measurements with Fy-2 alone, unlike in the RNA cross-linking studies, we observed that RNA binding was almost entirely abrogated ([Figures 5D](#) and [S7B](#)). It is

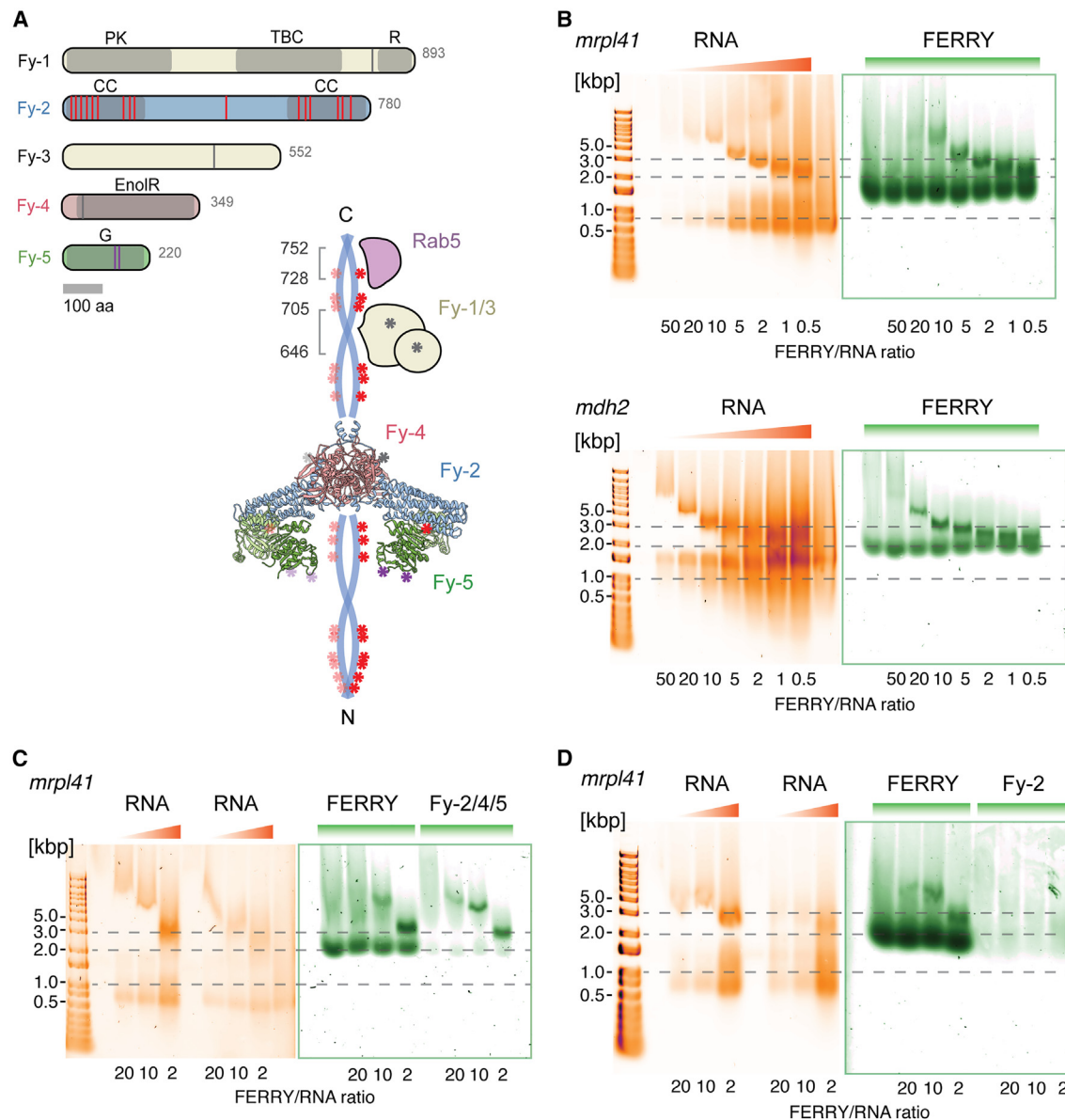


Figure 5. RNA binding of the FERRY complex

(A) Domain organization of FERRY subunits with positions of UV-crosslinks indicated. PK, pseudokinase; TBC, Tre-2/Bub2/Cdc16; R, rhodanese; CC, coiled-coil; EnolR, enoyl reductase; G, GATase1-like domain. Positions of UV-crosslinks between RNA/Fy-2 and RNA/Fy-5 are indicated by red and lilac asterisks, respectively. Crosslinks with RNA in the other FERRY subunits are indicated by gray asterisks. Only crosslinks are shown that were identified in at least 3 out of 5 replicates.

(B) EMSAs showing the interaction between FERRY and *mrp141* and *mdh2* mRNA in the upper and lower panel. RNA is stained with SYBR Gold (orange, left) and protein with Sypro Red (green, right).

(C) EMSAs showing that both, FERRY and the 3-subunit Fy-2/4/5 complex, are capable of binding the mRNA *mrp141* *in vitro*.

(D) EMSAs showing that in contrast to the fully assembled FERRY complex, Fy-2 alone is not sufficient to bind *mrp141* mRNA. See Figure S7 and Data S1.

possible that Fy-2 alone may not be able to adopt the correct conformation/folding to fulfill its function as RNA interactor as in the presence of Fy-4 and Fy-5.

To test this hypothesis and determine whether the coiled-coil domains of Fy-2 constitute indeed the main RNA binding site, we reconstituted different FERRY complexes of Fy-2 variants, in

which the N-terminal coiled-coil had been gradually truncated (Figures 6A, 6B, and 6D). EMSAs of these FERRY complexes showed that their RNA binding ability decreased almost proportionally with the length of the coiled-coil region, indicating that the coiled-coils indeed comprise the main RNA binding site of Fy-2 (Figure 6F). Thus, Fy-4 and Fy-5, which do not exhibit

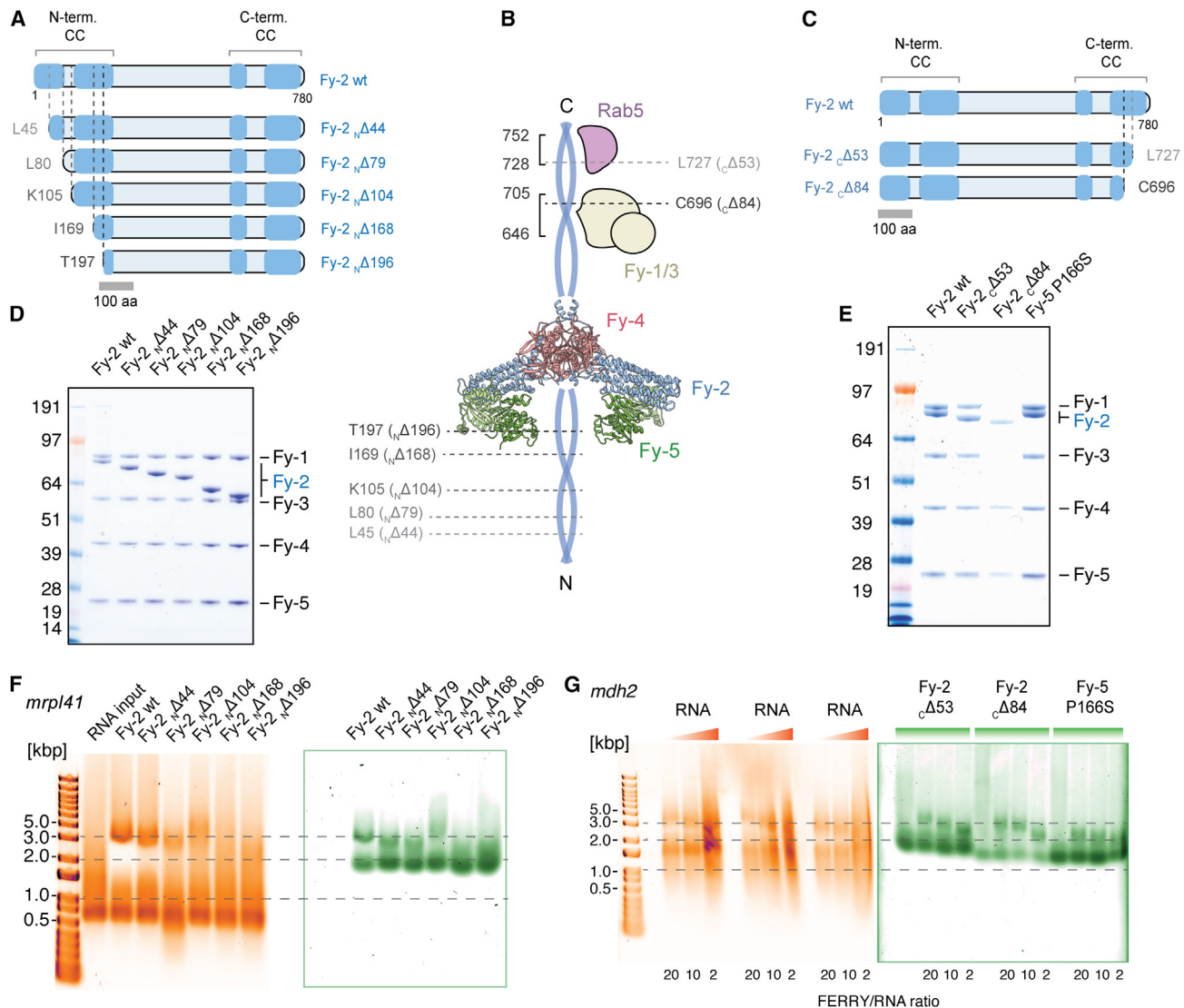


Figure 6. Coiled-coil domains of Fy-2 are essential for RNA binding

(A) Overview of N-terminal truncation variants of Fy-2. Predicted coiled-coil regions are highlighted in blue. (B) Schematic representation of FERRY with positions of N- and C-terminal truncations indicated by dashed lines. (C) Overview of C-terminal truncation variants of Fy-2. Predicted coiled-coil regions are highlighted in blue. (D and E) SDS-PAGE of reconstituted FERRY complex having the wt Fy-2 subunit replaced by either N-terminal (D) or C-terminal (E) truncation variants. (F and G) EMSAs showing the interaction between *mrp141* (F) and *mdh2* (G) mRNA and FERRY with Fy-2 being replaced by either N-terminal (F) or C-terminal (G) truncation variants. RNA is stained with SYBR Gold (orange, left) and protein with Sypro Red (green, right). See [Figures S5](#) and [S7](#).

detectable RNA binding ability on their own ([Figure S7D](#)), likely act as a stabilizer and scaffold for the proper orientation of the coiled-coils of Fy-2.

Together, these results demonstrate that although Fy-5 is part of a complex mRNA binding interface on the FERRY complex, the majority of interactions are mediated by the coiled-coils of Fy-2, which are structurally stabilized by Fy-4 and Fy-5.

To assess the number of mRNA molecules bound to FERRY, we performed mass photometry experiments with FERRY in the absence and presence of *mdh2* RNA ([Figure S5E](#)). We

measured an overall mass of 501 ± 25 kDa for the FERRY complex alone, corresponding well to the calculated molecular weight of 521 kDa. Considering that the mass was estimated based on protein standards, the measured molecular weight of *mdh2* RNA alone is as well close to the calculated value (722 kDa versus 655 ± 29 kDa). Upon FERRY-RNA complex formation, we observed an additional peak at $1,282 \pm 52$ kDa, likely corresponding to a 1:1 FERRY-*mdh2* RNA complex. Since we did not observe peaks at higher molecular mass, we interpret that one RNA molecule binds to a FERRY complex at a time *in vitro*.

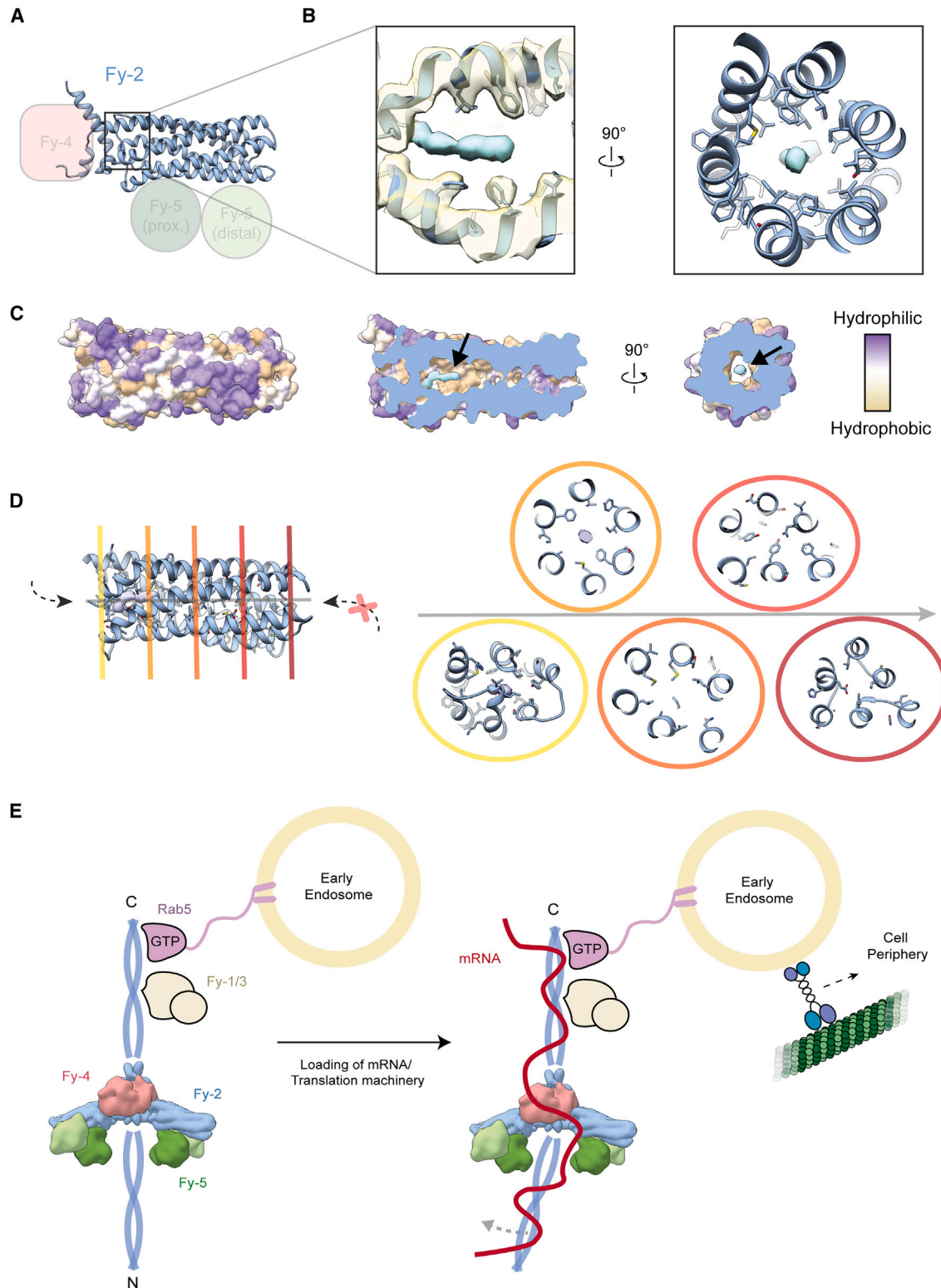


Figure 7. Hydrophobic binding pocket and model of FERRY recruitment and RNA binding

(A) The 6-helix bundle domain of Fy-2.

(B) Enlarged views of the interior of the 6-helix bundle domain at the Fy-4-facing end of the tube, as indicated in (A). Both 3D-reconstruction (semi-transparent) and fitted atomic model (blue) are shown. An additional, elongated density (cyan) is accommodated within the hollow cavity formed by the 6-helix bundle.

(legend continued on next page)

Disease-relevant mutations of FERRY

Our structural and functional knowledge of FERRY allows us to analyze further the molecular basis of disease-associated mutations of the FERRY complex. In a 2018 study, the homozygous nonsense variant c.2089C>T (p.Arg697*), which results in a truncated Fy-2 protein lacking the last 84 residues, was identified in a patient with a developmental and neurological disorder.⁴⁵ To investigate whether this mutation affects Fy-1/3 binding and the interaction with Rab5 as suggested by our HDX-MS studies (Figure 4A), we reconstituted and analyzed two FERRY variants with C-terminal deletion mutations in Fy-2, i.e., Fy-2_{Δ53} and Fy-2_{Δ84} (Figures 6B, 6C, 6E, and 6G). The first mutant lacks the region that was identified as the Rab5 binding site, whereas the second mutant also partially lacks the region identified as main Fy-1/3 interface (Figures 6B and 6C). The reconstitution of both complexes revealed that while Fy-2_{Δ53} together with the other proteins formed a stable five subunit complex, Fy-2_{Δ84} lacks the ability to interact with Fy-1 and Fy-3, resulting in a three-subunit core complex, i.e., Fy-2_{Δ84}/Fy-4/5 (Figure 6E). Both complexes showed no impairment in RNA binding (Figure 6G).

We additionally performed GST-Rab5 pull-down assays to examine Rab5 binding with the described FERRY mutant complexes (Figure S5D). While the variant lacking the C-terminal 84 residues completely abrogated Rab5 binding, the Fy-2_{Δ53} mutant displayed residual Rab5 binding, indicating that the Δ53 truncation included most but not the entire Rab5 interface. This suggests that the Rab5 binding interface identified by HDX (725–752) is indeed correct but must probably be extended by several residues toward the N terminus. Taken together, the disease-related C-terminal truncation of Fy-2 (Δ84) is impaired in FERRY complex assembly and also unable to bind Rab5, most likely resulting in severe misregulation of mRNA localization and transport.

For Fy-5, the point mutation P166S has been associated with gastric adenocarcinoma (<https://cancer.sanger.ac.uk>). This particular mutation is located in the Fy-2 binding region of Fy-5 and could hence disrupt complex formation. To better understand the molecular effect of this mutation, we introduced the point mutation (P166S) into Fy-5 and reconstituted a FERRY complex. We did not observe any impairment of FERRY assembly and RNA binding compared with the wild-type complex *in vitro* (Figures 6E, 6G, and S7C). This could mean that the disturbances caused by this mutation are either too subtle to be picked up by these *in vitro* assays or interfere with other processes unrelated to complex formation and mRNA transport *in vivo*. The association with gastric adenocarcinoma would suggest this since aberrant mRNA localization or transport causes primarily neuronal symptoms and brain dysfunction.

Hydrophobic cavity in the 6-helix bundle of Fy-2

The 6-helix bundle of Fy-2 connects Fy-4 with the Fy-5 dimer (Figure 7A). To our surprise, we identified an elongated density within the 6-helix bundle, located at its Fy-4-facing side (Figure 7B). While the exterior of the 6-helix bundle is mostly polar, its interior is highly enriched with hydrophobic residues (Figures 7B and 7C). This suggests that the elongated density, which is centered almost perfectly within the hydrophobic cavity, i.e., residing on the central tube axis, probably corresponds to a hydrophobic molecule. When we analyzed the arrangement of the six helices that constitute the tube in more detail, we observed a change in their organization along the central axis (Figure 7D). Starting from a hexagonal pattern on the Fy-4-facing side, they transition *en route* toward a more pyramidal-like arrangement on the opposite end. This rearrangement is accompanied by a gradual decrease of the intraluminal diameter of the tube. Consequently, the putative molecule could not access the tube from the “pyramidal” side unless major rearrangement occurred in the 6-helix bundle. Entering from the Fy-4-facing side therefore appears to be the more likely scenario, but would still require the displacement of one or more nearby loop regions of the 6-helix bundle, i.e., interleukin-1 (IL-1) and/or IL-2, in order to grant access to the hydrophobic interior. Another possible function of the hydrophobic moiety could be to support and facilitate the assembly of the FERRY complex, for example by stabilizing the 6-helix bundle of Fy-2. The implications of this unidentified molecule on the function of the FERRY complex are not immediately obvious and represent an interesting topic for further investigations.

DISCUSSION

In this study, we resolved the core of the Rab5 effector FERRY complex to 4.0 Å resolution using single-particle cryo-EM, revealing a unique architecture that does not resemble that of any known protein complex. Thus, FERRY represents a class of RNA-binding protein complex that exhibits an unusual mode of mRNA binding, involving the two terminal coiled-coils of the central Fy-2 subunit as well as Fy-5. None of the FERRY subunits contains a previously identified RNA-binding motif or domain,⁴⁶ and most of the interactions with RNA are mediated by the coiled-coils of Fy-2, providing an unusual mRNA binding hub.

Our crosslinking-MS and EMSA studies indicated that the bound RNA stretches over the entire length of the FERRY complex. The composite binding interface, comprising different FERRY subunits, might be necessary to create different binding specificities for various mRNA transcripts *in vivo*. The three-dimensional arrangement of possible RNA-binding sites likely determines the specificity and binding affinity of certain RNA

(C) Surface hydrophobicity of the 6-helix bundle domain of Fy-2. Cross sections of different orientations (middle, right panel) highlight the hydrophobic nature of the interior cavity, with position of the elongated density indicated by an arrow.

(D) Different cross sections of the 6-helix bundle domain of Fy-2 (right panel) with their respective position along the gray central tube axis indicated (left panel).

(E) Model of FERRY recruitment and RNA binding: activated GTP-bound Rab5 recruits FERRY by binding to the C-terminal coiled-coil of Fy-2. Since Rab5 proteins insert via two C-terminal lipidated cysteines into the EE membrane, FERRY also becomes EE-associated. FERRY interacts with mRNA and/or the translation machinery, with a single RNA molecule bound to the coiled-coils of Fy-2. The flexibility of the N-terminal coiled-coil might facilitate RNA binding via the FERRY clamp. Ultimately, motor protein-mediated transport of EEs via the MT network delivers the FERRY-associated RNA cargo to its respective cellular target destination.

molecules. Accordingly, EMSAs showed that binding affinities to FERRY varied between different RNA transcripts.

Together, our results allowed us to suggest the following mode of FERRY recruitment and loading (Figure 7E), where activated EE-associated Rab5 recruits the FERRY complex through binding to the C-terminal coiled-coil region of Fy-2 to the EE. The Rab5 binding site is located adjacent to the Fy-1 and Fy-3 subunits, which also bind to the C-terminal coiled-coil region. Because there is no obvious additional binding site for EE proteins on FERRY, we believe that the elongated complex sits with its long axis at 90° to the EE surface. However, it should be borne in mind that the connection of the Rab5 globular domain to the membrane is unlikely to be rigid, due to the poorly ordered long hypervariable domain of the GTPase C terminus in the absence of further interactions.^{47,48–51} Interestingly, the structure of the FERRY core resembles that of an RNA-binding clamp, raising the question whether this structure has mechanical implications. We observed a certain level of flexibility in the arms of the clamp in cryo-EM (Figure S3; Videos S1 and S2) indicating that the structural movements necessary for slight opening and closing of the clamp are possible. In addition, since the N-terminal coiled-coil of Fy-2 is—to a certain degree—flexible, it could facilitate the binding of the RNA by providing space inside the clamp. However, we propose that rather than mechanically clamping the RNA, the adaptable large three-dimensional (3D) cavity of the clamp provides the optimal binding site for structurally flexible RNAs. As shown by our truncation studies, the quite long coiled-coils of Fy-2 provide additional binding sites for RNA, thereby increasing the specificity and/or affinity for the cargo. FERRY binds a single RNA molecule as indicated by our mass photometry data (Figure 7E). Although we demonstrated that RNA binds directly to FERRY, we cannot exclude that additional adaptor proteins are involved in this process *in vivo*. The long N-terminal coiled-coil of Fy-2 would provide enough space for their binding.

Mutations in Fy-1 cause intellectual disability and severe infantile syndromic encephalopathy in patients, both characterized by brain atrophy.^{52,53} Mutations in Fy-3 have also been linked to intellectual disability, based on genetic analysis of two families.⁵⁴ For Fy-2, several mutations connected to malfunction of the brain have been described including four biallelic loss of function variants linked to neurodevelopmental syndrome.⁴⁷ Our study allowed us to show that both complex assembly and Rab5 binding are impaired in a 84 C-terminal residue-lacking homozygous Fy-2 nonsense variant, which was identified in a patient with developmental delay and brain abnormalities.⁴⁵ Our structural studies suggest that this results in a failure of FERRY to bind to EE via Rab5 *in vivo*, further underlining the importance of these subunits for the proper action of FERRY-mediated RNA transport. So far, no mutations have been described for Fy-4. There is the possibility that point mutations in this protein, despite its central position in the FERRY complex have less severe effects on the function of FERRY since it serves mainly as scaffold.

Another question that arises is the function of the density that we identified in the hydrophobic pocket formed by the 6-helix bundle of Fy-2. Due to the hydrophobic environment, we assume that the density corresponds to a hydrophobic molecule. While we can exclude detergents or similar amphipathic compounds

since these were not added during purification, it is also rather unlikely to represent a post-translational modification due to the unfavorable local environment. Binding of hydrophobic molecules to other RNA-binding proteins has been described before, including the natural product hippuristanol and mono-unsaturated fatty acids associated with the stem-cell translation regulator Musashi-1, mainly resulting in the inhibition of their respective RNA binding activity.^{48,49,55} We cannot exclude that the unknown hydrophobic molecule exerts a similar inhibitory effect on the RNA binding activity of FERRY. However, this scenario is rather unlikely since the main RNA-binding regions of the FERRY complex are located on the terminal coiled-coils of Fy-2 and, therefore, far away from the hydrophobic moiety. In addition, we observed RNA binding to FERRY in the presence of the hydrophobic moiety.

Taken together, our structural and functional analyses of FERRY extend the understanding of this remarkable Rab5 effector complex and hence also shed light onto how intracellular mRNA transport processes are coordinated within the cell, serving as a basis for future research.

Limitations of the study

Although we gained valuable insights into the architecture of FERRY by resolving its central core using cryo-EM, there is still a lot to learn about this fascinating RNA-binding complex. While HDX-MS and mutational studies allowed us to map the positions of the two unresolved subunits Fy-1/3 and Rab5 on Fy-2, the inherent flexibility of its terminal coiled-coils impeded a more comprehensive analysis of the interfaces. Furthermore, our study identified a previously undescribed mode for RNA binding. Subsequent studies will need to be performed to further unravel the molecular and functional determinants of mRNA interaction with FERRY.

STAR★METHODS

Detailed methods are provided in the online version of this paper and include the following:

- KEY RESOURCES TABLE
- RESOURCE AVAILABILITY
 - Lead contact
 - Materials availability
 - Data and code availability
- EXPERIMENTAL MODEL AND STUDY DETAILS
- METHOD DETAILS
 - Molecular cloning
 - Virus production and insect cell expression
 - Protein expression and purification
 - GST-Rab5 pulldown assays
 - *In vitro* transcription (IVT) and mRNA purification
 - Electrophoretic motility shift assays (EMSA)
 - Mass photometry
 - Crystallization of Fy-4 and Fy-5
 - Data collection, structure determination and analysis
 - Hydrogen-deuterium exchange mass spectrometry
 - UV-light induced protein-RNA crosslinking
 - Protein-protein crosslinking

- High pH reversed-phase chromatography
- Peptide size-exclusion chromatography
- LC-ESI-MS/MS and data analysis
- Rotary shadowing
- Sample vitrification
- Cryo-EM data acquisition
- Image processing and 3D reconstruction
- Model building, refinement and validation
- Hierarchical classification of 2D classes
- Structure analysis and visualization
- **QUANTIFICATION AND STATISTICAL ANALYSIS**

SUPPLEMENTAL INFORMATION

Supplemental information can be found online at <https://doi.org/10.1016/j.molcel.2023.05.009>.

ACKNOWLEDGMENTS

We thank O. Hofnagel and D. Prumbaum for assistance with EM data collection, M. Stabrin for lively discussions regarding image processing and M. Raabe for help with MS of crosslinked samples. We also acknowledge R. Goody and A. Musacchio for valuable feedback regarding the manuscript. We thank the protein expression and purification facility of the MPI-CBG for their support and the members of the cluster of excellence “Physics of Life” (EXC-2068–390729961) for stimulating discussion. This research was financially supported by the Deutsche Forschungsgemeinschaft - Project Number 112927078 - TRR 83 (to M.Z.) and the Max Planck Society (to S.R., M.Z. and H.U.).

AUTHOR CONTRIBUTIONS

J.S.S., S.R. and M.Z. designed the project. J.S.S. provided the protein complex and performed X-ray studies. J.S.S. and J.L. performed the HDX-MS experiments. L.M.W. and H.U. performed and analyzed crosslinking-MS experiments and P.J.H. performed low-angle platinum shadowing experiments. D.Q. prepared specimens, recorded, analyzed and processed EM data and prepared figures. T.R.S. performed hierarchical classification analysis. D.Q. and B.U.K. built the atomic models. S.R. managed the project. D.Q. and S.R. wrote the manuscript with input from all authors.

DECLARATION OF INTERESTS

The authors declare no competing interests.

INCLUSION AND DIVERSITY

We support inclusive, diverse, and equitable conduct of research.

Received: July 22, 2022

Revised: December 5, 2022

Accepted: May 5, 2023

Published: June 1, 2023

REFERENCES

1. Pfeffer, S.R. (2017). Rab GTPases: Master regulators that establish the secretory and endocytic pathways. *Mol. Biol. Cell* **28**, 712–715.
2. Wandinger-Ness, A., and Zerial, M. (2014). Rab proteins and the compartmentalization of the endosomal system. *Cold Spring Harb. Perspect. Biol.* **6**, 022616.
3. Zerial, M., and McBride, H. (2001). Rab proteins as membrane organizers. *Nat. Rev. Mol. Cell Biol.* **2**, 107–117.
4. Grosshans, B.L., Ortiz, D., and Novick, P. Rabs and their effectors: achieving specificity in membrane traffic. In *Proceedings of the National Academy of Sciences*, pp. 11821–11827.
5. Woodman, P.G. (2000). Biogenesis of the sorting endosome: the role of Rab5. *Traffic* **1**, 695–701.
6. Horiuchi, H., Lippé, R., McBride, H.M., Rubino, M., Woodman, P., Stenmark, H., Rybin, V., Wilm, M., Ashman, K., Mann, M., and Zerial, M. (1997). A novel Rab5 GDP/GTP exchange factor complexed to Rabaptin-5 links nucleotide exchange to effector recruitment and function. *Cell* **90**, 1149–1159.
7. Tall, G.G., Barbieri, M.A., Stahl, P.D., and Horazdovsky, B.F. (2001). Ras-activated endocytosis is mediated by the Rab5 guanine nucleotide exchange activity of RIN1. *Dev. Cell* **1**, 73–82.
8. Lanzetti, L., Rybin, V., Malabarba, M.G., Christoforidis, S., Scita, G., Zerial, M., and Di Fiore, P.P. (2000). The Eps8 protein coordinates EGF receptor signalling through Rac and trafficking through Rab5. *Nature* **408**, 374–377.
9. Haas, A.K., Fuchs, E., Kopajtich, R., and Barr, F.A. (2005). A GTPase-activating protein controls Rab5 function in endocytic trafficking. *Nat. Cell Biol.* **7**, 887–893.
10. Miaczynska, M., Christoforidis, S., Giner, A., Shevchenko, A., Uttenweiler-Joseph, S., Habermann, B., Wilm, M., Parton, R.G., and Zerial, M. (2004). APPL proteins link Rab5 to nuclear signal transduction via an endosomal compartment. *Cell* **116**, 445–456.
11. Nielsen, E., Christoforidis, S., Uttenweiler-Joseph, S., Miaczynska, M., Dewitte, F., Wilm, M., Hoflack, B., and Zerial, M. (2000). Rabenosyn-5, a novel Rab5 effector, is complexed with hVPS45 and recruited to endosomes through a FYVE finger domain. *J. Cell Biol.* **151**, 601–612.
12. Schnatwinkel, C., Christoforidis, S., Lindsay, M.R., Uttenweiler-Joseph, S., Wilm, M., Parton, R.G., and Zerial, M. (2004). The Rab5 effector Rabankyrin-5 regulates and coordinates different endocytic mechanisms. *PLoS Biol.* **2**, 261.
13. Stenmark, H., Vitale, G., Ullrich, O., and Zerial, M. (1995). Rabaptin-5 is a direct effector of the small GTPase Rab5 in endocytic membrane fusion. *Cell* **83**, 423–432.
14. Stenmark, H., Aasland, R., Toh, B.H., and D’Arrigo, A. (1996). Endosomal localization of the autoantigen EEA1 is mediated by a zinc-binding FYVE finger. *J. Biol. Chem.* **271**, 24048–24054.
15. Eathiraj, S., Pan, X., Ritacco, C., and Lambright, D.G. (2005). Structural basis of family-wide Rab GTPase recognition by rabenosyn-5. *Nature* **436**, 415–419.
16. Jagoe, W.N., Lindsay, A.J., Read, R.J., McCoy, A.J., McCaffrey, M.W., and Khan, A.R. (2006). Crystal structure of rab11 in complex with rab11 family interacting protein 2. *Structure* **14**, 1273–1283.
17. Zhu, G., Zhai, P., Liu, J., Terzyan, S., Li, G., and Zhang, X.C. (2004). Structural basis of Rab5-Rabaptin5 interaction in endocytosis. *Nat. Struct. Mol. Biol.* **11**, 975–983.
18. Chou, H.-T., Dukovski, D., Chambers, M.G., Reinisch, K.M., and Walz, T. (2016). CATCHR, HOPS and CORVET tethering complexes share a similar architecture. *Nat. Struct. Mol. Biol.* **23**, 761–763.
19. Kim, Y.-G., Raunser, S., Munger, C., Wagner, J., Song, Y.-L., Cygler, M., Walz, T., Oh, B.-H., and Sacher, M. (2006). The architecture of the multisubunit TRAPP I complex suggests a model for vesicle tethering. *Cell* **127**, 817–830.
20. Hoepfner, S., Severin, F., Cabezas, A., Habermann, B., Runge, A., Gillooly, D., Stenmark, H., and Zerial, M. (2005). Modulation of Receptor Recycling and Degradation by the Endosomal Kinesin KIF16B. *Cell* **121**, 437–450. <https://doi.org/10.1016/j.cell.2005.02.017>.
21. Medioni, C., Mowry, K., and Besse, F. (2012). Principles and roles of mRNA localization in animal development. *Development* **139**, 3263–3276.
22. Bröcker, C., Kuhlee, A., Gatsogiannis, C., Balderhaar, H.J.K., Hönscher, C., Engelbrecht-Vandré, S., Ungermann, C., and Raunser, S. (2012). Molecular architecture of the multisubunit homotypic fusion and vacuole

- protein sorting (HOPS) tethering complex. *Proc. Natl. Acad. Sci. USA* **109**, 1991–1996.
23. Das, S., Vera, M., Gandin, V., Singer, R.H., and Tutucci, E. (2021). Intracellular mRNA transport and localized translation. *Nat. Rev. Mol. Cell Bio.* **22**, 483–504. <https://doi.org/10.1038/s41580-021-00356-8>.
 24. Mofatteh, M. (2020). mRNA localization and local translation in neurons. *AIMS Neurosci.* **7**, 299–310.
 25. Vazquez-Pianzola, P., and Suter, B. (2012). Conservation of the RNA transport machineries and their coupling to translation control across eukaryotes. *Comp. Funct. Genomics* **2012**, 287852–287913.
 26. Martin, K.C., and Ephrussi, A. (2009). mRNA Localization: Gene Expression in the Spatial Dimension. *Cell* **136**, 719–730. <https://doi.org/10.1016/j.cell.2009.01.044>.
 27. Buxbaum, A.R., Haimovich, G., and Singer, R.H. (2015). In the right place at the right time: visualizing and understanding mRNA localization. *Nat. Rev. Mol. Cell Bio.* **16**, 95–109. <https://doi.org/10.1038/nrm3918>.
 28. Cioni, J.-M., Lin, J.Q., Holtermann, A.V., Koppers, M., Jakobs, M.A.H., Azizi, A., Turner-Bridger, B., Shigeoka, T., Franze, K., Harris, W.A., and Holt, C.E. (2019). Late Endosomes Act as mRNA Translation Platforms and Sustain Mitochondria in Axons. *Cell* **176**, 56–72.e15.
 29. Higuchi, Y., Ashwin, P., Roger, Y., and Steinberg, G. (2014). Early endosome motility spatially organizes polysome distribution. *J. Cell Biol.* **204**, 343–357. <https://doi.org/10.1083/jcb.201307164>.
 30. Liao, Y.-C., Fernandopulle, M.S., Wang, G., Choi, H., Hao, L., Drerup, C.M., Patel, R., Qamar, S., Nixon-Abell, J., Shen, Y., et al. (2019). RNA Granules Hitchhike on Lysosomes for Long-Distance Transport, Using Annexin A11 as a Molecular Tether. *Cell* **179**, 147–164.e20. <https://doi.org/10.1016/j.cell.2019.08.050>.
 31. Zarnack, K., and Feldbrügge, M. (2010). Microtubule-dependent mRNA transport in fungi. *Eukaryot. Cell* **9**, 982–990.
 32. De Vos, K.J., and Hafezparast, M. (2017). Neurobiology of axonal transport defects in motor neuron diseases: Opportunities for translational research? *Neurobiol. Dis.* **105**, 283–299.
 33. Parton, R.G., Simons, K., and Dotti, C.G. (1992). Axonal and dendritic endocytic pathways in cultured neurons. *J. Cell Biol.* **119**, 123–137. <https://doi.org/10.1083/jcb.119.1.123>.
 34. Goto-Silva, L., McShane, M.P., Salinas, S., Kalaizidis, Y., Schiavo, G., and Zerial, M. (2019). Retrograde transport of Akt by a neuronal Rab5-APPL1 endosome. *Sci. Rep.* **9**, 2433. <https://doi.org/10.1038/s41598-019-38637-0>.
 35. Schuhmacher, J.S., Dieck, S. tom, Christoforidis, S., Landerer, C., Gallesio, L., Seifert, S., Schäfer, R., Giner, A., Toth-Petroczy, A., et al. (2023). The Rab5 effector FERRY links early endosomes with mRNA localization. *Mol. Cell.* <https://doi.org/10.1016/j.molcel.2023.05.012>.
 36. Maier, T., Jenni, S., and Ban, N. (2006). Architecture of mammalian fatty acid synthase at 4.5 Å resolution. *Sci. New York N Y* **311**, 1258–1262. <https://doi.org/10.1126/science.1123248>.
 37. Szklarczyk, D., Franceschini, A., Wyder, S., Forslund, K., Heller, D., Huerta-Cepas, J., Simonovic, M., Roth, A., Santos, A., Tsafou, K.P., et al. (2015). STRING v10: protein–protein interaction networks, integrated over the tree of life. *Nucleic Acids Res.* **43**, D447–D452. <https://doi.org/10.1093/nar/gku1003>.
 38. Mishra, A., Eathiraj, S., Corvera, S., and Lambright, D.G. (2010). Structural basis for Rab GTPase recognition and endosome tethering by the C2H2 zinc finger of Early Endosomal Autoantigen 1 (EEA1). *Proc. Natl. Acad. Sci. USA* **107**, 10866–10871.
 39. Shi, Z., Gao, H., Bai, X.-C., and Yu, H. (2020). Cryo-EM structure of the human cohesin-NIPBL-DNA complex. *Science* **368**, 1454–1459.
 40. Lee, S.J., Kim, S.J., Kim, I.K., Ko, J., Jeong, C.S., Kim, G.H., Park, C., Kang, S.O., Suh, P.G., Lee, H.S., and Cha, S.S. (2003). Crystal structures of human DJ-1 and Escherichia coli Hsp31, which share an evolutionarily conserved domain. *J. Biol. Chem.* **278**, 44552–44559.
 41. van der Brug, M.P., Blackinton, J., Chandran, J., Hao, L.-Y., Lal, A., Mazan-Mamczarz, K., Martindale, J., Xie, C., Ahmad, R., Thomas, K.J., et al. (2008). RNA binding activity of the recessive parkinsonism protein DJ-1 supports involvement in multiple cellular pathways. *Proc. Natl. Acad. Sci. USA* **105**, 10244–10249. <https://doi.org/10.1073/pnas.0708518105>.
 42. Kramer, K., Sachsenberg, T., Beckmann, B.M., Qamar, S., Boon, K.-L., Hentze, M.W., Kohlbacher, O., and Urlaub, H. (2014). Photo-cross-linking and high-resolution mass spectrometry for assignment of RNA-binding sites in RNA-binding proteins. *Nat. Methods* **11**, 1064–1070. <https://doi.org/10.1038/nmeth.3092>.
 43. Ghaemi, Z., Guzman, I., Gnutt, D., Luthey-Schulten, Z., and Gruebele, M. (2017). Role of Electrostatics in Protein-RNA Binding: The Global vs the Local Energy Landscape. *J. Phys. Chem. B* **121**, 8437–8446.
 44. Lunde, B.M., Moore, C., and Varani, G. (2007). RNA-binding proteins: modular design for efficient function. *Nat. Rev. Mol. Cell Biol.* **8**, 479–490.
 45. Suleiman, J., Al Hashem, A.M., Tabarki, B., Al-Thihli, K., Bi, W., El-Hattab, A.W., and El-Hattab, A.W. (2018). PPP1R21 homozygous null variants associated with developmental delay, muscle weakness, distinctive facial features, and brain abnormalities. *Clin. Genet.* **94**, 351–355.
 46. Corley, M., Burns, M.C., and Yeo, G.W. (2020). How RNA-Binding Proteins Interact with RNA: Molecules and Mechanisms. *Mol. Cell* **78**, 9–29. <https://doi.org/10.1016/j.molcel.2020.03.011>.
 47. Rehman, A.U., Najafi, M., Kambouris, M., Al-Gazali, L., Makrythanasis, P., Rad, A., Maroofian, R., Rajab, A., Stark, Z., Hunter, J.V., et al. (2019). Biallelic loss of function variants in PPP1R21 cause a neurodevelopmental syndrome with impaired endocytic function. *Hum. Mutat.* **40**, 267–280.
 48. Gencic, R., and Pelletier, J. (2016). Hippuristanol - A potent steroid inhibitor of eukaryotic initiation factor 4A. *Transl. A*, e1137381. <https://doi.org/10.1080/21690731.2015.1137381>.
 49. Clingman, C.C., Deveau, L.M., Hay, S.A., Genga, R.M., Shandilya, S.M.D., Massi, F., and Ryder, S.P. (2014). Allosteric inhibition of a stem cell RNA-binding protein by an intermediary metabolite. *Elife* **3**, e02848. <https://doi.org/10.7554/elifelife.02848>.
 50. Kabsch, W. (2010). *Acta Crystallogr. D Biol. Crystallogr.* **66**, 125–132.
 51. Winn, M.D., Ballard, C.C., Cowtan, K.D., Dodson, E.J., Emsley, P., Evans, P.R., Keegan, R.M., Krissinel, E.B., Leslie, A.G.W., McCoy, A., et al. (2011). Overview of the CCP4 suite and current developments. *Acta Crystallogr. D Biol. Crystallogr.* **67**, 235–242.
 52. Bhoj, E.J., Li, D., Harr, M., Edvardson, S., Elpeleg, O., Chisholm, E., Juusola, J., Douglas, G., Guillen Sacoto, M.J., Siquier-Pernet, K., et al. (2016). Mutations in TBCK, Encoding TBC1-Domain-Containing Kinase, Lead to a Recognizable Syndrome of Intellectual Disability and Hypotonia. *Am. J. Hum. Genet.* **98**, 782–788.
 53. Chong, J.X., Caputo, V., Phelps, I.G., Stella, L., Worgan, L., Dempsey, J.C., Nguyen, A., Leuzzi, V., Webster, R., Pizzuti, A., et al. (2016). Recessive Inactivating Mutations in TBCK, Encoding a Rab GTPase-Activating Protein, Cause Severe Infantile Syndromic Encephalopathy. *Am. J. Hum. Genet.* **98**, 772–781.
 54. Philips, A.K., Pinelli, M., de Bie, C.I., Mustonen, A., Määttä, T., Arts, H.H., Wu, K., Roepman, R., Moilanen, J.S., Raza, S., et al. (2017). Identification of C12orf4 as a gene for autosomal recessive intellectual disability. *Clin. Genet.* **91**, 100–105.
 55. Bordeleau, M.-E., Mori, A., Oberer, M., Lindqvist, L., Chard, L.S., Higa, T., Belsham, G.J., Wagner, G., Tanaka, J., and Pelletier, J. (2006). Functional characterization of IRESes by an inhibitor of the RNA helicase eIF4A. *Nat. Chem. Biol.* **2**, 213–220. <https://doi.org/10.1038/nchembio776>.
 56. McCoy, A.J., Grosse-Kunstleve, R.W., Adams, P.D., Winn, M.D., Storoni, L.C., and Read, R.J. (2007). Phaser crystallographic software. *J. Appl. Crystallogr.* **40**, 658–674.
 57. Emsley, P., and Cowtan, K.; IUCr (2004). Coot: model-building tools for molecular graphics. *Acta Crystallogr. D Biol. Crystallogr.* **60**, 2126–2132.

58. Adams, P.D., Afonine, P.V., Bunkóczy, G., Chen, V.B., Davis, I.W., Echols, N., Headd, J.J., Hung, L.-W., Kapral, G.J., Grosse-Kunstleve, R.W., et al. (2010). PHENIX: a comprehensive Python-based system for macromolecular structure solution. *Acta Crystallogr. D Biol. Crystallogr.* **66**, 213–221.
59. Pascal, B.D., Willis, S., Lauer, J.L., Landgraf, R.R., West, G.M., Marciano, D., Novick, S., Goswami, D., Chalmers, M.J., and Griffin, P.R. (2012). HDX Workbench: Software for the Analysis of H/D Exchange MS Data. *J. Am. Soc. Mass Spectrom.* **23**, 1512–1521.
60. Yang, B., Wu, Y.-J., Zhu, M., Fan, S.-B., Lin, J., Zhang, K., Li, S., Chi, H., Li, Y.-X., Chen, H.-F., et al. (2012). Identification of cross-linked peptides from complex samples. *Nat. Methods* **9**, 904–906. <https://doi.org/10.1038/nmeth.2099>.
61. Kosinski, J., von Appen, A., Ori, A., Karius, K., Müller, C.W., and Beck, M. (2015). Xlink Analyzer: Software for analysis and visualization of cross-linking data in the context of three-dimensional structures. *J. Struct. Biol.* **189**, 177–183. <https://doi.org/10.1016/j.jsb.2015.01.014>.
62. Pettersen, E.F., Goddard, T.D., Huang, C.C., Couch, G.S., Greenblatt, D.M., Meng, E.C., and Ferrin, T.E. (2004). UCSF Chimera—a visualization system for exploratory research and analysis. *J. Comput. Chem.* **25**, 1605–1612. <https://doi.org/10.1002/jcc.20084>.
63. Stabrin, M., Schoenfeld, F., Wagner, T., Pospich, S., Gatsogiannis, C., and Raunser, S. (2020). TranSPHIRE: automated and feedback-optimized on-the-fly processing for cryo-EM. *Nat. Commun.* **11**, 5716. <https://doi.org/10.1038/s41467-020-19513-2>.
64. Zheng, S.Q., Palovcak, E., Armache, J.-P., Verba, K.A., Cheng, Y., and Agard, D.A. (2017). MotionCor2: anisotropic correction of beam-induced motion for improved cryo-electron microscopy. *Nat. Methods* **14**, 331–332.
65. Moriya, T., Saur, M., Stabrin, M., Merino, F., Voicu, H., Huang, Z., Penczek, P.A., Raunser, S., and Gatsogiannis, C. (2017). High-resolution Single Particle Analysis from Electron Cryo-microscopy Images Using SPHIRE. *J. Vis. Exp.* 55448 <https://doi.org/10.3791/55448>.
66. Rohou, A., and Grigorieff, N. (2015). CTFFIND4: Fast and accurate defocus estimation from electron micrographs. *J. Struct. Biol.* **192**, 216–221. <https://doi.org/10.1016/j.jsb.2015.08.008>.
67. Wagner, T., Merino, F., Stabrin, M., Moriya, T., Antoni, C., Apelbaum, A., Hagel, P., Sitsel, O., Raisch, T., Prumbaum, D., et al. (2019). SPHIRE-crYOLO is a fast and accurate fully automated particle picker for cryo-EM. *Commun. Biol.* **2**, 218. <https://doi.org/10.1038/s42003-019-0437-z>.
68. Scheres, S.H.W. (2012). RELION: implementation of a Bayesian approach to cryo-EM structure determination. *J. Struct. Biol.* **180**, 519–530. <https://doi.org/10.1016/j.jsb.2012.09.006>.
69. Ramlal, K., Palmer, C.M., Nakane, T., and Aylett, C.H.S. (2020). Mitigating local over-fitting during single particle reconstruction with SIDESPLITTER. *J. Struct. Biol.* **211**, 107545.
70. Ramlal, K., Palmer, C.M., and Aylett, C.H.S. (2019). A Local Agreement Filtering Algorithm for Transmission EM Reconstructions. *J. Struct. Biol.* **205**, 30–40.
71. Yang, J., Anishchenko, I., Park, H., Peng, Z., Ovchinnikov, S., and Baker, D. (2020). Improved protein structure prediction using predicted interresidue orientations. *Proc. Natl. Acad. Sci USA* **117**, 1496–1503. <https://doi.org/10.1073/pnas.1914677117>.
72. Shaikh, T.R., Gao, H., Baxter, W.T., Asturias, F.J., Boisset, N., Leith, A., and Frank, J. (2008). SPIDER image processing for single-particle reconstruction of biological macromolecules from electron micrographs. *Nat. Protoc.* **3**, 1941–1974.
73. Tang, G., Peng, L., Baldwin, P.R., Mann, D.S., Jiang, W., Rees, I., and Ludtke, S.J. (2007). EMAN2: an extensible image processing suite for electron microscopy. *J. Struct. Biol.* **157**, 38–46.
74. Young, S.J., and Lin, Z.D. (2018). Ethanol gas sensors based on multi-wall carbon nanotubes on oxidized Si substrate. *Microsyst. Technol.* **24**, 55–58. <https://doi.org/10.1007/s00542-016-3154-2>.
75. Lauer, J., Segeletz, S., Cezanne, A., Guaitoli, G., Raimondi, F., Gentzel, M., Alva, V., Habeck, M., Kalaidzidis, Y., Ueffing, M., et al. (2019). Auto-regulation of Rab5 GEF activity in Rabex5 by allosteric structural changes, catalytic core dynamics and ubiquitin binding. *Elife* **8**, e46302.
76. Mayne, L., Kan, Z.-Y., Chetty, P.S., Ricciuti, A., Walters, B.T., and Englander, S.W. (2011). Many Overlapping Peptides for Protein Hydrogen Exchange Experiments by the Fragment Separation-Mass Spectrometry Method. *J. Am. Soc. Mass Spectrom.* **22**, 1898–1905.
77. Walters, B.T., Ricciuti, A., Mayne, L., and Englander, S.W. (2012). Minimizing back exchange in the hydrogen exchange-mass spectrometry experiment. *J. Am. Soc. Mass Spectrom.* **23**, 2132–2139.
78. Huis In 't Veld, P.J., Jeganathan, S., Petrovic, A., Singh, P., John, J., Krenn, V., Weissmann, F., Bange, T., and Musacchio, A. (2016). Molecular basis of outer kinetochore assembly on CENP-T. *Elife* **5**, e21007. <https://doi.org/10.7554/elife.21007>.
79. Wagner, T., and Raunser, S. (2020). The evolution of SPHIRE-crYOLO particle picking and its application in automated cryo-EM processing workflows. *Commun. Biol.* **3**, 61. <https://doi.org/10.1038/s42003-020-0790-y>.
80. Pettersen, E.F., Goddard, T.D., Huang, C.C., Couch, G.S., Greenblatt, D.M., Meng, E.C., and Ferrin, T.E. (2004). UCSF Chimera—A visualization system for exploratory research and analysis. *J. Comput. Chem.* **25**, 1605–1612.
81. Liebschner, D., Afonine, P.V., Baker, M.L., Bunkóczy, G., Chen, V.B., Croll, T.I., Hintze, B., Hung, L.W., Jain, S., McCoy, A.J., et al. (2019). Macromolecular structure determination using X-rays, neutrons and electrons: recent developments in Phenix. *Acta Crystallogr. D Struct. Biol.* **75**, 861–877.
82. Yang, Z., Fang, J., Chittuluru, J., Asturias, F.J., and Penczek, P.A. (2012). Iterative stable alignment and clustering of 2D transmission electron microscope images. *Structure* **20**, 237–247. <https://doi.org/10.1016/j.str.2011.12.007>.
83. Frank, J., Radermacher, M., Penczek, P., Zhu, J., Li, Y., Ladjadi, M., and Leith, A. (1996). SPIDER and WEB: processing and visualization of images in 3D electron microscopy and related fields. *J. Struct. Biol.* **116**, 190–199.
84. Baxter, W.T., Leith, A., and Frank, J. (2007). SPIRE: the SPIDER reconstruction engine. *J. Struct. Biol.* **157**, 56–63.

STAR★METHODS

KEY RESOURCES TABLE

REAGENT or RESOURCE	SOURCE	IDENTIFIER
Bacterial and virus strains		
<i>E. coli</i> BL21 (DE3)	In-house made	N/A
<i>E. coli</i> DH5 α	In-house made	N/A
Insect cell baculovirus	In-house made	N/A
Chemicals, peptides, and recombinant proteins		
SYBR™ Gold Nucleic Acid Gel Stain	Invitrogen	Cat# S33102
SYPRO Red Protein Gel Stain	Sigma Aldrich	Cat# S6654
ESF 921 Insect Cell Culture Medium	Expression Systems	Cat# 96-001
Critical commercial assays		
T7 RiboMAX™ Express Large Scale RNA Production System	Promega	Cat# P1320
QIAprep Spin Miniprep Kit	Qiagen	Cat# 27106
QIAquick PCR Purification Kit	Qiagen	Cat# 28106
Deposited data		
Cryo-EM density map of FERRY	This paper	EMD: 12273
Model coordinates of FERRY	This paper	PDB: 7ND2
X-ray model coordinates of Fy-4	This paper	PDB: 83AO
X-ray model coordinates of Fy-4	This paper	PDB: 83AP
FERRY MS proteomics data	This paper	PXD034875
Mendeley Dataset including uncropped gels	This paper	https://doi.org/10.17632/7v3rsntjfx.1
Experimental models: Cell lines		
Sf9 cells	Expression systems	Cat#94-001F
Oligonucleotides		
mRNA <i>mdh2</i> ; sequence see 'method details' section	This paper	N/A
mRNA <i>mrp141</i> ; sequence see 'method details' section	This paper	N/A
mRNA <i>prdx5</i> ; sequence see 'method details' section	This paper	N/A
mRNA <i>pig1</i> ; sequence see 'method details' section	This paper	N/A
Recombinant DNA		
Fy-5 (N-His, pOCC1)	Schuhmacher et al., 2023 ³⁵	N/A
Fy-4 (N-His, pOCC5)	Schuhmacher et al., 2023 ³⁵	N/A
Fy-1 (N-His), Fy-2 and Fy-3 (pOEM, multi-gene construct)	Schuhmacher et al., 2023 ³⁵	N/A
Rab5a (N-His, N-GST, pGAT2)	Schuhmacher et al., 2023 ³⁵	N/A
GST-Rab5a (N-GST, pGEX-6P-3)	Schuhmacher et al., 2023 ³⁵	N/A
pUC57 <i>syn-mrp141</i> -mRNA	Schuhmacher et al., 2023 ³⁵	N/A
pUC57 <i>syn-mdh2</i> -mRNA	Schuhmacher et al., 2023 ³⁵	N/A
pUC57 <i>syn-prdx5</i> -mRNA	Schuhmacher et al., 2023 ³⁵	N/A
pUC57 <i>syn-pig1</i> -mRNA	Schuhmacher et al., 2023 ³⁵	N/A
GST-Fy-2 (pOCC151)	This paper	N/A
Fy-2 (N-His), Fy-4 (N-His) and Fy-5 (N-His) (pOEM, multi-gene construct)	This paper	N/A
Fy-1 (N-His), Fy-2 (45–780) and Fy-3 (pOEM, multi-gene construct)	This paper	N/A

(Continued on next page)

Continued

REAGENT or RESOURCE	SOURCE	IDENTIFIER
Fy-1 (N-His), Fy-2 (80–780) and Fy-3 (pOEM, multi-gene construct)	This paper	N/A
Fy-1 (N-His), Fy-2 (105–780) and Fy-3 (pOEM, multi-gene construct)	This paper	N/A
Fy-1 (N-His), Fy-2 (169–780) and Fy-3 (pOEM, multi-gene construct)	This paper	N/A
Fy-1 (N-His), Fy-2 (197–780) and Fy-3 (pOEM, multi-gene construct)	This paper	N/A
Fy-1 (N-His), Fy-2 (1–696) and Fy-3 (pOEM, multi-gene construct)	This paper	N/A
Fy-1 (N-His), Fy-2 (1–727) and Fy-3 (pOEM, multi-gene construct)	This paper	N/A
Fy-5 P166S (N-His, pOCC1)	This paper	N/A

Software and algorithms

XDS	Kabsch, 2010 ⁵⁰	https://xds.mr.mpg.de
CCP4/SCALA	Winn et al., 2011 ⁵¹	https://www.ccp4.ac.uk/html/scala.html
CCP4/PHASER	McCoy et al., 2007 ⁵⁶	https://www.ccp4.ac.uk/html/phaser.html
COOT	Emsley et al., 2004 ⁵⁷	https://www2.mrc-lmb.cam.ac.uk/personal/pemsley/coot/
PHENIX	Adams et al., 2010 ⁵⁸	https://phenix-online.org
HDX workbench	Pascal et al., 2012 ⁵⁹	https://hdxworkbench.com
OpenMS	Kramer et al., 2014 ⁴²	https://openms.de
xiNET	Yang et al., 2012 ⁶⁰	https://xiview.org/xiNET_website/
Xlink Analyzer tool	Kosinski et al., 2015 ⁶¹	https://www.embl-hamburg.de/XlinkAnalyzer/XlinkAnalyzer.html
UCSF Chimera	Pettersen et al., 2004 ⁶²	https://www.cgl.ucsf.edu/chimera/
TranSPHIRE	Stabrin et al., 2020 ⁶³	https://github.com/MPI-Dortmund/transpire
MotionCor2	Zheng et al., 2017 ⁶⁴	https://emcore.ucsf.edu/ucsf-software
SPHIRE	Moriya et al., 2017 ⁶⁵	https://sphire.mpg.de
CTFFIND4	Rhou and Grigorieff, 2015 ⁶⁶	https://grigoriefflab.umassmed.edu/ctffind4
SPHIRE-crYOLO	Wagner et al., 2019 ⁶⁷	https://cryolo.readthedocs.io
RELION	Scheres et al., 2012 ⁶⁸	https://www3.mrc-lmb.cam.ac.uk/relion
SIDESPLITTER	Ramlal et al., 2020 ⁶⁹	https://github.com/StructuralBiology-ICLMedicine/SIDESPLITTER
L-AFTER	Ramlal et al., 2019 ⁷⁰	https://github.com/StructuralBiology-ICLMedicine/lafter
trRosetta	Yang et al., 2020 ⁷¹	https://yanglab.nankai.edu.cn/trRosetta
SPIDER	Shaikh et al., 2008 ⁷²	https://github.com/spider-em/SPIDER
EMAN2	Tang et al., 2007 ⁷³	https://blake.bcm.edu/emanwiki/EMAN2

RESOURCE AVAILABILITY

Lead contact

Further information and requests for resources and reagents should be directed to and will be fulfilled by the Lead Contacts, Stefan Raunser (stefan.raunser@mpi-dortmund.mpg.de) and Marino Zerial (zerial@mpi-cbg.de)

Materials availability

This study did not generate new unique reagents.

Data and code availability

- The cryo-EM density map of the FERRY complex is deposited into the Electron Microscopy DataBank with the accession number EMD: 12273. Model coordinates for the FERRY complex, the X-ray structures of Fy-4 and Fy-5 are available with the PDB

entry IDs PDB: 7ND2, PDB: 8A3O and PDB: 8A3P, respectively. The mass spectrometry proteomics data have been deposited to the ProteomeXchange Consortium via the PRIDE partner repository with the dataset identifier PXD034875.

- This paper does not report original code.
- Any additional information required to reanalyze the data reported in this paper is available from the [lead contact](#) upon request.

EXPERIMENTAL MODEL AND STUDY DETAILS

Bacterial strains: Recombinant proteins were expressed in *Escherichia coli* BL21 (DE3) under autoinduction conditions using D-(+)-lactose monohydrate supplemented with the respective antibiotics at 30°C.

Insect cell lines: Sf9 cells were cultured in ESF921 media (Expression Systems) at 27°C for expression of baculovirus.

METHOD DETAILS

Molecular cloning

The human proteins Fy-1 (Tbck, ENSG00000145348, Q8TEA7), Fy-2 (Ppp1r21, ENSG00000162869, Q6ZMI0), Fy-3 (C12orf4, ENSG0000047621, Q9NQ89), Fy-4 (Cryz1, ENSG00000205758, O95825), Fy-5 (Gatd1, ENSG00000177225, Q8NB37) and Rab5a (ENSG00000144566, P20339) were used in vectors as described.³⁵ Fy-4 and Fy-5 were expressed with a non-cleavable N-terminal hexahistidine (His₆) tag in bacteria and insect cells, respectively. Fy-1, Fy-2 and Fy-3 were combined in multi-gene plasmid with Fy-1 carrying an N-terminal His₆ tag and produced in insect cells. Rab5 was used as GST fusion variant in a pGEX-6P-3 or pGAT2 vector. For C-terminal truncation mutants of Fy-2 and the Fy-5 P166S mutant the respective fragments were ordered from a commercial supplier (Twist Bioscience) and introduced into the respective vectors/constructs. The fragments for the N-terminal truncation mutants of Fy-2 were amplified by PCR and introduced into the FERRY multi-gene construct replacing *wildtype* Fy-2. To obtain a Fy-2/Fy-4/Fy-5 complex, all three proteins were introduced into a multi-gene construct with all three proteins carrying an N-terminal hexahistidine (His₆) tag.

Virus production and insect cell expression

Sf9 cells growing in ESF921 media (Expression Systems) were co-transfected with linearized viral genome and the expression plasmid and selected for high infectivity. P1 and P2 viruses were generated according to the manufacturer's protocol. Best viruses were used to infect Sf9 cells at 10⁶ cells/mL at 1% v/v and routinely harvested after 40–48 h at about 1.5x10⁶ cells/ml. The pellet was suspended in lysis buffer (20 mM HEPES, pH 8.0, 250 mM NaCl, 20 mM KCl, 20 mM MgCl₂ and 40 mM imidazole) or SEC buffer (20 mM HEPES, pH 7.5, 250 mM NaCl, 20 mM KCl and 20 mM MgCl₂) supplemented with a protease inhibitor cocktail, flash frozen in liquid nitrogen and stored at –80°C.

Protein expression and purification

The FERRY complex, its individual components Fy-4 and Fy-5 and Rab5 were essentially expressed and purified as described in Schuhmacher et al.³⁵ For better readability a brief description of the expression and purification is given in the following.

In general, purified proteins were analyzed using SDS-PAGE and their concentration determined by spectrophotometer (NanoDrop Lite, Thermo Scientific) unless stated.

Fy-5 and GST-Rab5

Fy-5, Fy-5 P166S and GST-Rab5 (from pGAT2) were expressed in *E. coli* BL21 (DE3) under autoinduction conditions using D-(+)-lactose monohydrate at 1.75% (w/v), supplemented with the respective antibiotics (50 µg/mL kanamycin or 100 µg/mL ampicillin) at 30°C. Harvested bacteria were suspended in lysis buffer and subsequently lysed or stored at –80°C. After lysis (sonication) the protein was purified from the clarified lysate in a two-step purification, involving Ni-NTA affinity chromatography (HisTrap FF column, GE Healthcare) and size exclusion chromatography (SEC) (HiLoad 16/600 Superdex 200 pg, GE Healthcare) in SEC buffer.

Fy-4

After sonication and clarification of the lysate by centrifugation (22 500 rpm/61 236 x g, 20 min, 4°C), the lysate was filtrated using Millex HV membrane filter units with a pore size of 0.45 µm (Merck Millipore). Fy-4 was subsequently purified combining Ni-NTA affinity chromatography (HisTrap FF column, GE Healthcare) and SEC (HiLoad 16/600 Superdex 200 pg, GE Healthcare).

Fy-2

Fy-2 was expressed as N-terminal GST fusion variant (GST-Fy-2) in Sf9 cells. Insect cells were harvested by centrifugation, resuspended in SEC buffer (20 mM HEPES (pH 7.5), 250 mM NaCl, 20 mM KCl and 20 mM MgCl₂) containing 1% Triton X-100 and lysed by flash freezing in liquid nitrogen and thawing. The lysate was clarified by centrifugation (22 500 rpm/61 236 x g, 20 min, 4°C) and supplemented with Glutathione Sepharose 4B (Cytiva, 2.0 mL resin/1 L insect cell pellet) and incubated for 1.5 h at 4°C on a rotating wheel. The resin was washed and 3 times with SEC buffer. The protein was cleaved from resin by addition of HRV 3C protease (produced in house) and incubation o/n at 4°C. The resulting protein was further purified by SEC without concentration using a Superdex 200 column (HiLoad 16/600 Superdex 200 pg, GE Healthcare) equilibrated in SEC buffer. Protein containing fractions were pooled

and concentrated according to experimental requirements. Concentration was determined by a spectrophotometer (NanoDrop Lite, Thermo Scientific).

Fy-2/Fy-4/Fy-5 complex

A Fy-2/Fy-4/Fy-5 complex was reconstituted by expressing the individual subunits from a single virus in Sf9 cells. Insect cells were harvested by centrifugation, resuspended in lysis buffer (20 mM HEPES (pH 7.5), 250 mM NaCl, 20 mM KCl and 20 mM MgCl₂) and by flash freezing in liquid nitrogen for storage. Melted cell pellets were lysed using sonication and the lysate clarified by centrifugation (22 500 rpm/61 236 x g, 20 min, 4°C). The resulting clarified lysate was supplemented with Ni-NTA agarose (Qiagen, 1.0 mL resin/1 L insect cell pellet) and incubated for 30 min at 4°C. Subsequently, the resin was transferred into gravity flow chromatography columns (Poly-Prep Chromatography Column, Bio-Rad) and extensively washed with lysis buffer. The Fy-2/Fy-4/Fy-5 complex was eluted with elution buffer (20 mM HEPES, pH 7.5, 250 mM NaCl, 20 mM KCl, 20 mM MgCl₂ and 500 mM imidazole) in 0.6 mL fractions and protein containing fractions were applied to SEC without further concentration using a Superose 6 increase column (Superose 6 Increase 10/300 GL, GE Healthcare) that was equilibrated in SEC buffer.

FERRY complex

To reconstitute the FERRY complex or the respective FERRY variants, Fy-1 to Fy-3 were expressed from a single virus and the harvested insect cells supplemented with purified Fy-4 and Fy-5 prior to cell lysis (Microfluidizer LM20, Microfluidics). The purification was accomplished by combining affinity chromatography and SEC. After clarification (22 500 rpm/61 236 x g, 20 min, 4°C) and filtration (Millex HV membrane filter units), the lysate was supplemented with Ni-NTA agarose (Qiagen, 1.3 mL resin/1 L insect cell pellet). Subsequently, the resin was transferred into gravity flow chromatography columns (Poly-Prep Chromatography Column, Bio-Rad) and extensively washed with lysis buffer and wash buffer (20mM HEPES, pH 7.5, 250mM NaCl, 20mM KCl, 20mM MgCl₂ and 80mM imidazole). The complex was eluted with elution buffer (20 mM HEPES, pH 7.5, 250 mM NaCl, 20 mM KCl, 20 mM MgCl₂ and 500 mM imidazole) in 1 mL fractions and protein containing fractions were applied to SEC without further concentration using a Superose 6 increase (Superose 6 Increase 10/300 GL, GE Healthcare) which was equilibrated in SEC buffer.

Rab5

Expression of GST-Rab5 was performed under autoinduction conditions as described for Fy-5. Harvested bacterial pellets were re-suspended in SEC buffer, lysed using sonication and the lysate clarified by centrifugation (22 500 rpm/61 236 x g, 20 min, 4°C). GST-Rab5 was captured on Glutathione Sepharose 4B resin (Cytiva), extensively washed with SEC buffer and cleaved off the resin using HRV 3C protease (produced in house). The protein was subsequently concentrated using Amicon Ultracel-30K (Millipore) centrifuge filters and applied to SEC using a Superdex 200 column (HiLoad 16/600 Superdex 200 pg, GE Healthcare) equilibrated in SEC buffer.

Rab5 was loaded with GTP γ S prior to the HDX experiments. To do so, Rab5 was concentrated using an Amicon Ultracel-30K (Millipore) centrifuge filter, subsequently supplemented with 2.5 mM GTP γ S and 250 nM of a GST fusion of the Rab5 GEF domain of Rabex5 and incubated for 60 min on ice. To remove the Rab5 GEF domain, Glutathione Sepharose 4B was added to the mixture and incubated for 90 min at 4°C. The resin was pelleted by centrifugation (12 000 rpm/15 300 x g, 10 min, 4°C) and the supernatant containing the GTP γ S loaded Rab5 was flash frozen and stored at -80°C. The protein concentration was determined using a BCA assay (Pierce BCA Protein Assay Kit, Thermo Scientific).

GST-Rab5 pulldown assays

Direct GST-Rab5 interaction assays were performed as described in Schuhmacher et al.³⁵ In brief, 12 μ L Glutathione Sepharose 4B (Cytiva) was saturated with 5 nmol GST-Rab5 and unbound protein removed. The beads were incubated with 1 mM nucleotide (GDP or GTP γ S) and 420 nM of GST-Rabex5-Vps9 for 60 min at 4°C to achieve nucleotide loading. After washing, 0.2 nmol of FERRY or the different FERRY variants were added to the beads in a total volume of 100 μ L and incubated for 20 min at 4°C on a shaker (700 rpm). After extensive washing, proteins were eluted with SEC buffer supplemented with 20 mM GSH and analyzed by SDS-PAGE.

In vitro transcription (IVT) and mRNA purification

mRNA sequences for *mdh2*, *mrl41*, *prdx5* and *pigl* comprise the coding region, the 3' and 5' untranslated regions (UTRs) and an additional polyA appendix of 50 adenines.

mdh2

aatacgaactactataGggacttccccgtcaccagctcctgtgctgcccagtcgggtgccctcccgtccagccatgctctccgccctcgcccggcctgccagcgctgctctcc
gcccagcttcagcactcggccagaacaatgctaaagtactgtgctaggggctcggaggcatcggcagccacttcacttctcgaagaacagccccttggtgagcc
gcctgaccctctatgatatcgcgcacacaccggagtgccgcagatctgagccacatcgagaccaaacccgctgtgaaaggtaacctcggacctgaacagctgctgactg
cctgaaaggttgatgtgtagtattccggctggagtcaccagaagccaggcatgaccgggacgacctgtcaacaccaatgccagattgtggccaccctgaccgctgc
ctgtgccagcactgcccgaagccatgatctgcgtcattgccaatccggttaattccaccatccccatcacagcagaagtttcaagaagcattggagtgtaacacccaacaaa
atcttggcgtgacgaccctggacatctgacagccaacaccttggtagagctgaagggttgatccagctcagtcacagctccctgctattggtggccatgctggaagac
catcatcccctgatctcagtcaccaccaagtgagcttccccaggaccagctgacagcactcactggcgatccaggaggccggcagggaggtggtcaaggctaaa
gccggagcagctcgcaccctccatggcgtatccggcgcccgtttgtcttcccctgtggtgatcaatgaatggaaggaaggtgttggatgttccctcgttaagtcac
aggaaacggaatgtactcttccacaccgctgctgctgggaaagggcatcgagaagaacctgggcatcggcaaacgctcctctttgagggaagatgatctcgatgc
catccccgagctgaaggcctccatcaagaagggggaagatttcgtgaagaccctgaagtgagccgctgacgggtggccagtttccctaatatgaaggcatcatgtcactgc
aaagccgtgacagataaacttattttaaattgtttggtgatgattactgtattgacatcatcatgcttccaaattgtgggtgctctgtggcgcatcaataaagccgctctgatt
tattttcaaggtccctctgtaaatgctgtgcttctccctgtgagagccaactttagatgtctgctacctcttaccatcagaattagatgtttaaactgttagactgaagcgt

gacgcttcatcagtagctcaagaaagtctaattgtaattatggaattggacacagattcagttaccggtacatgctcctcccggcctcctgttggcacccttgcacgccc
ggcctgattcctcctggggtagttcacccccacgggttcagctcagcggcgaatgccaggcagctgtttctggctgagcaaacagcaccttctcattgagcttccctcactga
cctctgtccccctgggattcattctgacccaacccctgatgttcagtgccagagacagcccatagcagaactgtgggtagaccagggtgggggtgctgggttgggacagcc
caaacccagccgctgtgtcaaggcctaggacgcatgctgcatcaaaaggggttccagggttccatcagtgccctaaagaaggacttctgtgtactgaggagtgcggaa
taaagagattgactcccttagtattggggcagtcggtccccagacactgtggcctctgaagtggaaactgaaagctgcatactgggaagaacttctaggaataggcaat
ggcctcagtggaagaggagggtggaggtgtgccagttctggatgttcacacacagcttttggtttttaaaaaagctaaatggaatggatttatcataaaggat
gacatcgttttcttacaattaatacatgttcattgtataaacccaaaagcagctaaaaataaagcgggaagggaactactgtgtaaaaaaaaaaaaaaaaaaaaa
aaaaaaaaaaaaaaaaaaaaaaaaaaagcggccg.

mrpl41

taatacgactcactataGgggctcttctgctgcagcagcggctcgggaagcggagcaaggtcagggcgggtggcggcggagccggggcggcttggagctcgtgtgggctc
cggccaggggcggcctgggctgctggccgagcggcgcgctgctggctcgggggtgaggaccgaatgagcaagtgagcagcaagcggggcccgccgagctcagg
ggccgcaagggcgggggcccagggcatcggcttctcacctcgggctggaggtctgtgcagatcaaggagatggtcccggagttcgtctccggatctgaccggctca
agctcaagccctacgtgagctacctcggcctgagagcggagagcggcctgacggcggcgcagctctcagcgaagccgtggcctgcatacaaaaggactcaagg
acggtaccttgaccctgacaacctggaaaagtacggcttcgagcccacagggaggaaagctcttcagctcaccaggaaactcctgcgtagctgggagggggagg
ggcggcctgcctcattctattaaacgccttggcagctaaaaaaaaaaaaaaaaaaaaaaaaaaaaaaaaaaaaaaaaaaaaaaaaaaaaaaagcggccg.

prdx5

taatacgactcactataGgggctcgcaggggtgctgcgctgtgcccgtgagcgggtgcccgcctgctcgggtggcaccagccaggaggcggagtggaagtggcctggggc
gggtatgggactagctggcgtgtgcccctgagagcgtcagcgggctatatactcgtgggtggggccggcgtcagctgctggcagcggcagcaagacgggtacagtgaagga
gagtgggcgtctggcgggtccgcagttcagcagagccgctgcagccatggcccaatcaaggtgggagatgcatccagcagtgagggtgtggaaggggagccagg
aacaaggtgaacctggcagagctgtcaagggaagaaggggtgtgctgtttggagttcctgggctcaccctggatgttcaagacacacctgccagggttgggagcagg
ctgaggtctgaaggccaagggagtcaggtggtggcctgtctgagtgtaaatgatgcttctgactggcagtgaggggcggagccacagggcgaaggaaggtcggctcc
tggctgatcccactggggccttgggaaggagacagacttactatagatgattcgtggtgctcatcttgggaatcagctcctcaagagttctccatggtgtacaggtggcat
agtgaaggccctgaatgtggaaccagatggcacaggcctcacctgcagcctggcaccacaatcatctcacagctctgaggccctggccagattactctccaccctccct
atctcacctgccagccctgtgctggggccctgcaattggaatgtggccagattctgcaataaacactgtggtttggggcAAAAAAAAAAAAAAAAAAAAAAAAAAAA
AAAAAAAAAAAAAAAAAAAAAAAAAagcggccg.

pigl

taatacgactcactatagggagtgctgttaccatcatggaagcaatgtggctcctgtgtggtggcgttggcgttggcagtggggctcctctgggttgggactcctcagaacga
atgaagagtcgggagcagggagcagcgtgggagccgaaagccggaccctgctggtcatagcaccctgacgatgaagccatgttttctccacagtgctaggcttggc
ccgctaaggcactgggtgtacgtcttctctcaggaattactacaatcaaggagagactcgaagaagaacttttcagagctgtgatgtttgggattccactctcca
gtgtaatgattatgacaacagggatttccagatgaccaggcagctgagtgggacacagagcagctggccagagtcctcctcagcacatagaagtgaatggcatcaatctgtg
ggtagcttctgagcagggggagtaagtggccacagcaatcacattgctctgtatgcagctgtgagggccctgcactcagaaggaagttacataaagggtgctctgtgctcag
ctcagctgtgtaatgtgctgcgaagtagctccttctggatctgcccctgtctctcctacacgagcaggtatgctcctctgctcaacagcaaaagagtgccacaggccaaga
aagccatgctcctgccaccgagcagctcctctggttccgcccctctacattatcttcccggatagatgagaatcaactcactgagcttccctgaaagccttgaagggtttcaga
tccaaggaacaaaggggaaatagacaaaggagtcagaggacctggcctggcactggtatttacctgagctcaaggagatcccggctggagcagcctctgcaaaaggg
agcccatgtagccaggggtgtccaaactccagcttctcccctgggaaaaaacccaaagaacaaaaaacaccccaaggataataatagctacactgctagcttctc
aagttcttgtaaaaaaatattacataatgacacagtagatgtggaacacctgaccagtgctggcggcaggtccctattatcataatgaacataaaagtgtctaaaaaacctcca
cagatgtgactttacattgtttcaagcaggttcaaaaaacacatacacaatgcaacagtggtgttgaattggtcaatcataatccttggattttctgtatcagaatgtggg
tctaggaaaaaactgtctatttaacaggaaaaaaaaaaaaaaaaaaaaaaaaaaaaaaaaaaaaaaaaaaaaaaaaagcggccg.

mRNAs were produced by *in vitro* transcription (IVT) using the T7 RiboMAX Express Large Scale RNA Production System (Prom-ega) according to the manufacturer’s protocol. Resulting RNA was extracted and purified by a Phenol:Chloro-form extraction followed by an isopropanol precipitation as described in the manual of the mMESSAGE mMACHINE T7 Transcription kit (Thermo Fisher). The IVT reaction was quenched with Ammonium acetate stop solution (5M Ammonium acetate, 100 mM EDTA) and supplemented with Phenol:Chloro-form:Isoamyl Alcohol 25:24:1 (Sigma Aldrich). After recovery of the aqueous phase, it was supplemented with an equal amount of isopropanol. Subsequently the mixture was chilled at -20°C for at least 15 min and the precipitated RNA was pelleted by centrifugation (20 800 x g, 15 min, 4°C). After centrifugation the supernatant was removed and the pellet resuspended in RNase-free water. RNA concentrations were determined by a spectrophotometer (NanoDrop Lite, Thermo Scientific) and the RNA was stored at -80°C until usage.

Electrophoretic motility shift assays (EMSA)

For direct protein-RNA interaction assays, 10 pmol of FERRY complex (500 nM) or the respective FERRY variant complexes were mixed with *in vitro transcribed* mRNA (10 nM–1 μM) in varying protein/RNA ratios in SEC buffer in a total volume of 20 μL and incubated for 80 min at 37°C. The samples were analyzed using gel electrophoresis, RNA was visualized using SYBR Gold Nucleic Acid Gel Stain (Invitrogen) and proteins were stained using SYPRO Red Protein Gel Stain (Sigma Aldrich) according to the manufacturers’ protocols.

EMSA assays comparing the ability of Fy-5, Fy-4 and a mixture of Fy-5 and Fy-4 with the full FERRY complex shown in Figure S7D were performed with 90 pmol Fy-5 (2.57 μM), 45 pmol Fy-4 (1.3 μM), 90 pmol Fy-5 together with 45 pmol Fy-4 and 22.5 pmol of

FERRY complex (640 nM) and mixed with 15 pmol of *in vitro* transcribed *mrpl41* mRNA (430 nM) in SEC buffer in a total volume of 35 μ L. After an incubation of 80 min at 37°C the samples were analyzed using gel electrophoresis using 1% agarose gels and the RNA was visualized using ethidium bromide.

Mass photometry

For the mass photometry measurements 10 pmol FERRY complex was mixed with 10 pmol *in vitro* transcribed *mdh2* RNA in a total volume 20 μ L and incubated for 80 min at 37°C. The sample was diluted into SEC buffer to reach 100 nM prior to data acquisition. Mass Photometry (MP, iSCAMS) was performed on a TwoMP instrument (Refeyn, Oxford, UK) at room temperature. High precision 24 \times 50 mm coverslips (Thorlabs CG15KH) were cleaned with ultrasound, rinsed with isopropanol and water and dried with clean nitrogen gas⁷⁴ and coated with 0.01% Poly-L-lysine solution (Sigma, P4832). Mass calibration was performed using BSA, IgG, Thyroglobulin standards (Sigma), Low DNA Mass ladder (Invitrogen, 10068013) and Millenium RNA marker (ThermoFisher, AM7150) in MP buffer (20 mM HEPES, pH 7.4, 150 mM NaCl). 20 μ L diluted FERRY-RNA mixture (10 nM final in MP buffer) was spotted into a reusable culture well gasket with 3 mm diameter and 1 mm depth (Grace Bio-Labs). MP signals were recorded for 60 s and 120 s at a suitable concentration in order to detect a sufficient set of target particles (>500). Raw MP data were processed in the DiscoverMP software (Refeyn, Oxford, UK).

Crystallization of Fy-4 and Fy-5

All crystallization experiments were carried out by the sitting-drop method in SWISSCI MRC 2-well crystallization plates at room temperature with a reservoir volume of 50 μ L and a drop volume of 3 μ L, using a 1:1 mixture of protein and crystallization solution. Initial crystals of Fy-5 were obtained from a 15 mg/mL solution after 4–6 weeks in 0.1 M MES, pH 5.0, 0.8 M Ammonium sulfate. Fy-4 crystals were grown from a 12 mg/mL solution after 3–5 days in 0.1 M MES pH 6.0, 5% (w/v) PEG 3000 and 30% (w/v) PEG 200.

Data collection, structure determination and analysis

Crystals were flash-frozen in liquid nitrogen after a short incubation in a cryo-protecting solution composed of mother-liquor supplemented with 20% (v/v) glycerol. Data collection was performed at the European Synchrotron Radiation Facility (ESRF) in Grenoble, France under cryogenic conditions at the beamline: ID30A-3. Data were recorded with an EIGER X 4M detector. Diffraction data was processed using XDS⁵⁰ and the CCP4-implemented program SCALA.⁵¹ The structures of Fy-4 and Fy-5 were solved by molecular replacement (MR) with CCP4-integrated PHASER.⁵⁶ APC35852, a member of the DJ superfamily (pdb: 1u9c) was used as search model for Fy-5 and the NADP⁺ bound version of human zeta-crystallin (pdb: 1yb5) was used as search model to solve the structure of Fy-4. The structures were manually built in COOT⁵⁷ and refined using PHENIX refine.⁵⁸

Hydrogen-deuterium exchange mass spectrometry

HDX-MS was performed as previously described.^{75–77} Proteins (120 μ L of 0.5 μ M) are diluted 6:4 with 8 M urea, 1% trifluoroacetic acid, passed over an immobilized pepsin column (2.1 mm \times 30 mm, ThermoFisher Scientific) in 0.1% trifluoroacetic acid at 15°C. Peptides are captured on a reversed-phase C8 cartridge, desalted and separated by a Zorbax 300SB-C18 column (Agilent) at 1°C using a 5–40% acetonitrile gradient containing 0.1% formic acid over 10 min and electrosprayed directly into an Orbitrap mass spectrometer (LTQ-Orbitrap XL, ThermoFisher Scientific) with a T-piece split flow setup (1:400). Data were collected in profile mode with source parameters: spray voltage 3.4 kV, capillary voltage 40 V, tube lens 170 V, capillary temperature 170°C. MS/MS CID fragment ions were detected in centroid mode with an AGC target value of 104. CID fragmentation was 35% normalized collision energy (NCE) for 30 ms at Q of 0.25. HCD fragmentation NCE was 35eV. Peptides were identified using Mascot (Matrix Science) and manually verified to remove ambiguous peptides. For measurement of deuterium uptake, 12 μ L of 5 μ M protein was diluted in SEC buffer prepared with deuterated solvent. Samples were incubated for varying times at 22°C followed by the aforementioned digestion, desalting, separation and mass spectrometry steps. The intensity weighted average *m/z* value of a peptide's isotopic envelope was compared plus and minus deuteration using the HDX workbench software platform.⁵⁹ Individual peptides were verified by manual inspection. Data were visualized using Pymol. Deuterium uptake was normalized for back-exchange when necessary, by comparing deuterium uptake to a sample incubated in 6M urea in deuterated buffer for 12–18 h at room temperature and processed as indicated above.

UV-light induced protein-RNA crosslinking

The purified FERRY complex was reconstituted with *mrpl41* mRNA in equimolar amounts at 37°C for 1 h in 20 mM HEPES pH 7.5, 250 mM NaCl, 20 mM KCl, 20 mM MgCl₂. For reconstitution, the RNA/FERRY complex concentration was adjusted to 400 nM. Aliquots containing 125 pmol of the complex were UV-irradiated ($\lambda = 254$ nm) on ice for 10 min in an in-house built crosslinking apparatus following ethanol-precipitation.⁴² Further sample processing was performed as described with minor modifications.⁴² Briefly, the protein-RNA pellet was dissolved in 4 M urea, 50 mM Tris/HCl, pH 7.5 by sonication. For RNA digestion, the sample was diluted to 1 M urea with 50 mM Tris/HCl, pH 7.5 and 10 μ g RNase A (EN0531, Thermo Fisher Scientific) and 1kU RNase T1 (EN0531, Thermo Fisher Scientific) were added following incubation at 37°C for 4 h. Proteins were digested over night at 37°C with trypsin (V5111, Promega) at a 1:20 enzyme to protein mass ratio. Sample cleanup was performed using C18 columns (74–4601, Harvard Apparatus) according to the manufacturers' instructions and crosslinked peptides were enriched with TiO₂ columns (in-house; Titansphere 5 μ m; GL Sciences), as described.⁴² Peptide-(oligo)nucleotides were dried and subjected to LC-ESI-MS/MS.

Protein-protein crosslinking

For protein-protein crosslinking with EDC, purified FERRY complex was diluted to 400 nM complex concentration using buffer containing 250 mM NaCl, 20 mM KCl, 20 mM MgCl₂, 20 mM HEPES pH 6.7, 2 mM EDC and 0.5 mM Sulfo-NHS were added, following incubation at 30°C for 30 min. For quenching, 50 mM β-mercaptoethanol and 20 mM Tris-HCl, pH 7.5 were added. Samples were supplemented with 1 M urea and reduced by addition of 10 mM DTT and 30 min incubation at 37°C, following alkylation for 30 min at 25°C with 40 mM iodacetamide (IAA) and quenching of residual IAA by adding another 10 mM of DTT and incubation for 5 min at 37°C. Protein digestion was accomplished by overnight incubation at 37°C with trypsin (V5111, Promega) at a 1:20 enzyme to protein mass ratio. C18 columns (74–4601, Harvard Apparatus) were used for peptide clean-up according to the manufacturers' instructions. Crosslinked peptides were pre-fractionated by high pH reversed-phase chromatography or by peptide size exclusion chromatography.

High pH reversed-phase chromatography

EDC-crosslinked FERRY peptides were separated on a Xbridge C18 column (Cat. No. 186003128, Waters) using an Agilent 1100 series chromatography system. The system was operated at a flow rate of 60 μL/min with a buffer system comprising: buffer A: 10 mM NH₄OH; buffer B: 10 mM NH₄OH pH 10, 80% [v/v] acetonitrile (ACN). The following gradient was used for peptide separation: 5% buffer B (0–7 min), 8–30% buffer B (8–42 min), 30–50% buffer B (43–50 min), 90–95% buffer B (51–56 min), 5% buffer B (57–64 min). For the first 4 min, eluant was collected as flow-through fraction. For the following 48 min, 1-min fractions were collected and reduced to 12 fractions by concatenated pooling. After drying, samples were subjected to LC-MS/MS analysis.

Peptide size-exclusion chromatography

EDC-crosslinked FERRY peptides were separated on a Superdex Peptide PC3.2/3 0 column (GE Healthcare) at a flow rate of 50 μL min⁻¹. The system was operated in 30% [v/v] CAN, 0.1% [v/v] trifluoroacetic acid (TFA) for 60 min and 1-min fractions were collected. Vacuum-dried fractions were subjected to LC-MS/MS analysis.

LC-ESI-MS/MS and data analysis

Fractionated EDC-crosslinked peptides or enriched peptide-(oligo)nucleotides were dissolved in 2% [v/v] CAN, 0.05% [v/v] TFA. LC-MS/MS analyses were performed on an Orbitrap Exploris 480 (Thermo Scientific) instrument coupled to a nanoflow liquid chromatography system (Thermo Scientific Dionex Ultimate 3000). Sample separation was performed over 58 min at a flow rate of 300 nL/min using 0.1% [v/v] formic acid (FA) (buffer A) and 80% [v/v] CAN, 0.08% [v/v] FA (buffer B) and a linear gradient from 10% to 45% or to 46% buffer B in 44 min, for peptide-(oligo)nucleotides and EDC-crosslinked peptides, respectively. Eluting peptides were analyzed in positive mode using a data-dependent top 30 acquisition method. Resolution was set to 120,000 (MS1) and 30,000 FWHM (MS2). AGC targets were set to 1e6 (peptide-(oligo)nucleotides) or 3e6 (EDC-crosslinked peptides) for MS1 and 1e5 for MS2. Normalized collision energy was set to 28%, dynamic exclusion to 10 s (peptide-(oligo)nucleotides) or 30 s (EDC-crosslinked peptides), and maximum injection time to 60 ms (peptide-(oligo)nucleotides) or 'auto' (EDC-crosslinked peptides) for MS1 and 120 ms for MS2. For peptide-(oligo)nucleotide analyses, charge states 1 and ≥ 8 were excluded; for EDC-crosslinked peptide analyses, charge states 1, 2 and ≥ 8 were excluded from fragmentation. Measurements of peptide-(oligo)nucleotides were performed twice for the first technical replicate and once for second and third technical replicate; measurements of EDC-crosslinked peptide fractions were performed once.

Protein-RNA crosslink MS data were analyzed and manually validated using the OpenMS pipeline RNPxl and OpenMS TOPPAS-Viewer (<https://www.openms.de>), version 2.6.0.⁴² Methionine oxidation was set as variable modification, precursor mass tolerance was set to 6 ppm, maximum missed cleavages to 2, minimum peptide length to 5 amino acids, and maximum number of nucleotides was set to 3. We note that U-H₂O cannot be distinguished from C-NH₃ as these RNA adducts have the same monoisotopic masses.

EDC crosslink MS raw data files were converted to mgf format using Proteome Discoverer software (Thermo Scientific, version 2.1.0.81; signal-to-noise ratio: 1.5; precursor mass: 350–7000 Da). Crosslink peptide spectra were analyzed using pLink software (pFind group, version 1.23) choosing 'conventional crosslinking (HCD)' flow type and EDC-DE as linker. Oxidation of methionine was set as variable and carbamidomethylation of cysteine as fixed modification. Precursor mass tolerance was set to 10 ppm, maximum missed cleavages to 2 and minimum peptide length to 5 amino acids. Data were filtered for 1% crosslink spectrum match (CSM) FDR. Downstream analysis and crosslink visualization was performed using xiNET (https://xiview.org/xiNET_website/)⁶⁰ and Xlink Analyzer tool (version 1.1.2beta)⁶¹ in UCSF Chimera (<https://www.cgl.ucsf.edu/chimera/>, version 1.16).

Rotary shadowing

Low-angle metal shadowing and electron microscopy was performed as described previously.⁷⁸ In brief, freshly purified FERRY complexes were diluted 1:1 with spraying buffer (200 mM ammonium acetate and 60% glycerol) to a concentration of approximately 0.5 μM and air-sprayed onto freshly cleaved mica pieces (V1 quality, Plano GmbH). Specimens were mounted and dried in a MED020 high-vacuum metal coater (Bal-tec). A platinum layer of approximately 1 nm and a 7 nm carbon support layer were subsequently evaporated onto the rotating specimen at angles of 7° and 45°, respectively. Pt/C replicas were released from the mica on water, captured by freshly glow-discharged 400-mesh Pd/Cu grids (Plano GmbH), and visualized using a LaB₆ equipped JEM-1400 transmission electron microscope (JEOL) operated at 120 kV. Images were recorded at a nominal magnification of

60,000× on a 4k x 4k CCD camera F416 (TVIPS), resulting in 0.189 nm per pixel. Particles with discernible coiled-coil extensions were manually selected.

Sample vitrification

For sample preparation in cryo-EM, 3.5 μL of purified FERRY complex at a concentration of 0.7 mg/mL was applied to freshly glow-discharged UltrAuFoil 1.2/1.3 grids (Quantifoil), automatically blotted for 3 s and plunged into liquid ethane using the Vitrobot (Thermo Fisher Scientific), operated at 100% humidity and 13°C. Individual grid quality was screened prior to data collecting using a Talos Arctica transmission electron microscope (TEM, Thermo Fisher Scientific), operated at 200 kV. Prior to data collection, grids were stored in liquid nitrogen.

Cryo-EM data acquisition

Cryo-EM dataset of the FERRY complex was collected on a Titan Krios TEM (Thermo Fisher Scientific), equipped with an C_s-Corrector and in-column energy filter, operated at an acceleration voltage of 300 kV. Micrographs were recorded on a K2 direct electron detector (Gatan) with a final pixel size of 1.08 Å in counting mode. A total of 40 frames (with 375 ms and 1.895 e⁻/Å² each) was recorded during each exposure, resulting in a total exposure time of 15 s and an overall electron dose of 75.8 e⁻/Å². Automated data collection was done with the help of the software EPU (Thermo Fisher Scientific) and monitored in real time using TranSPHIRE.⁶³ A total of 1879 micrographs was collected with a defocus range between -1.6 μm and -2.8 μm and an energy filter width of 20 eV.

Image processing and 3D reconstruction

Initially, micrographs were inspected visually to discard images with high drift and ice-contamination. Using MotionCor2, operated in 3 x 3 patch mode, individual frames were aligned and summed.⁶⁴ In this step, unweighted and dose-weighted full-dose images were calculated. Image processing was performed with the SPHIRE software package (Table 1).⁶⁵ Values for the defocus and astigmatism of unweighted full-dose images were determined using CTFFIND4.⁶⁶ A flowchart of the image processing strategy is described in Figure S2. First, particles were automatically selected based on a trained model with the help of SPHIRE-crYOLO.^{67,79} After extraction of the particles with a window size of 264 x 264, the resulting stack was further classified using the iterative and stable alignment and clustering (ISAC) algorithm, implemented in SPHIRE. This yielded a stack of 18.5 k particles of dose-weighted drift-corrected particles. Based on a subset of class averages produced by ISAC, the *ab initio* 3D structure determination program RVIPER in SPHIRE calculated an initial intermediate resolution 3D structure that served as reference in the subsequent 3D refinement (MERIDIEN). This 3D refinement step, in which C2 symmetry was imposed, yielded a 5.9 Å map of the core of the FERRY complex, estimated by the 'gold standard' 0.143 criterion of the Fourier shell correlation (FSC). Based on the obtained 3D parameters, particles were re-centered, followed by re-extraction, resulting in 18.3 k particles. 3D refinements with C2 symmetry and without applying symmetry yielded 3D reconstruction with resolutions of 4.6 and 6.2 Å, respectively. In the next step, iterative cycles of Bayesian particle polishing in RELION⁶⁸ and 3D refinement in SPHIRE⁶⁵ were performed. The particles of this 'polished' stack were further subjected to another round of 3D refinement in SPHIRE with imposed C2 symmetry. Here, the real space filtering according to signal-to-noise ratio (SNR) algorithm, named SIDESPLITTER, was applied to reduce overfitting.⁶⁹ This resulted in a final 4.0 Å electron density map of the FERRY complex.

In general, the global resolution of maps was calculated between two independently refined half maps at the 0.143 criterion. Local resolutions were calculated with LOCALRES in SPHIRE. EM density maps were either filtered according to global resolution or using the local de-noising filter L-AFTER.⁷⁰ In the latter case, which is also based on half maps, features with more signal than noise are better recovered.

Model building, refinement and validation

To build the model for the (Fy-4)₂(Fy-2)₂(Fy-5)₄ core of the FERRY complex, the obtained crystal structures of Fy-4 and Fy-5 were initially fitted into the corresponding density using the rigid body fitting tool in Chimera.⁸⁰ trRosetta, a *de novo* protein structure prediction algorithm that is based on direct energy minimization with restrained Rosetta, was used to obtain initial models for Fy-2.⁷¹ The predicted model for the 6-helix bundle domain, containing residues 246 to 498, that matched our experimental density best was subsequently fitted similarly to Fy-4 and Fy-5 using rigid body fit. Manual model building for the regions N- and C-terminal 6-helix bundle, which comprise residues 218–245 and 499–552, respectively, was further guided by secondary structure predictions of individual trRosetta runs for these regions, which include the vertical helix as well as the beginning of the two terminal coiled-coils of Fy-2. With the resulting combined model, containing residues 2–349, 218–552 and 8–217 of Fy-4, Fy-2 and Fy-5, respectively, a restrained refinement in PHENIX was performed.⁸¹ In the next step, the model was further refined using a combination of manual building in COOT and real-space refinement in PHENIX.^{57,81} Geometries of the final model were either obtained from PHENIX or calculated using Molprobit (http://molprobit.biochem.duke.edu). Refinement and model building statistics are summarized in Table 1.

Hierarchical classification of 2D classes

Separate hierarchical classifications were run for classes selected from ISAC.⁸² Aligned particles from each class were generated using the SPHIRE program *sp_eval_isac.py* (http://sphire.mpg.de/wiki/doku.php?id=pipeline:utilities:sp_eval_isac). Particles for each class were then subjected to multivariate data analysis and hierarchical classification in SPIDER.^{72,83} Binary masks for

correspondence analysis were drawn manually onto class averages using *e2display.py* from EMAN2,⁷³ and then thresholded in SPIDER using the operation 'TH M'. Hierarchical classification using Ward's method was performed using SPIDER operation 'CL HC'. Class averages were visualized by the Python script *binarytree.py* which uses SPIDER's SPIRE libraries.⁸⁴ SPIDER procedures can be found at the SPIDER web site (<https://github.com/spider-em/SPIDER/tree/master/docs/techs/MSA>).

Structure analysis and visualization

UCSF Chimera was used for structure analysis, visualization and figure preparation.⁸⁰ The angular distribution plots as well as beautified 2D class averages were calculated in SPHIRE.⁶⁵

QUANTIFICATION AND STATISTICAL ANALYSIS

Statistical parameters are reported in figures and figure legends.